Optimization and assessment of phytoplankton size class algorithms for ocean color data on the Northeast U.S. continental shelf

Turner, Kyle J.[a,*], Mouw, Colleen B.[a], Hyde, Kimberly J. W.[b], Morse, Ryan[b], Ciochetto, Audrey B.[a]

[a]Graduate School of Oceanography, University of Rhode Island, 215 S. Ferry Rd., Narragansett, RI, 02882, USA

[b]Northeast Fisheries Science Center, National Oceanic and Atmospheric Administration, 28 Tarzwell Dr., Narragansett, RI, 02882, USA

[*] Corresponding author.

Email: kjturner@uri.edu (Kyle Turner)

Abstract

The size structure of phytoplankton communities influences important ecological and biogeochemical processes, including the transfer of energy through marine food webs. A variety of algorithms have been developed to estimate phytoplankton size classes (PSCs) from satellite ocean color data. However, many of these algorithms were developed for application to the global ocean, and their performance in more productive, optically complex coastal and continental shelf regions warrants evaluation. In this study, several existing PSC models were applied in the Northeast U.S. continental shelf (NES) region and compared with *in situ* PSC estimates derived from a local HPLC pigment data set. The effect of regional re-parameterization and incorporation of sea surface temperature (*SST*) into existing abundance-based model frameworks was investigated and model performance was assessed using an independent data set. Abundance-based model re-parameterization alone did not result in significant improvement in model performance compared with other models. However, the inclusion of *SST* led to a consistent reduction in model error for all size classes. Of two absorption-based algorithms tested, the best performing approach displayed similar performance metrics to the regional *SST*-dependent abundance-based model. The *SST*-dependent model and the absorption-based method were applied to monthly composites of the NES region for April and September 2019 and qualitatively compared. The results highlight the benefit of considering *SST* in abundance-based models and the applicability of absorption-based PSC methods in optically complex regions.

1. Introduction

Phytoplankton form the base of pelagic food webs and are a key component in biogeochemical cycles that ultimately impact global climate (Behrenfeld et al., 2006; Field et al., 1998). Phytoplankton in the ocean are taxonomically diverse and exhibit an array of unique morphological and physiological characteristics (Caron et al., 2012; Finkel et al., 2010). Phytoplankton community composition and biomass are highly variable in time and space, changing in response to both bottom-up (e.g., environmental conditions, nutrient availability) and top-down (e.g., grazing) controls. Understanding the dynamics of phytoplankton abundance and community structure is critical for studies of marine ecology and biogeochemistry.

Functional traits or groupings have been applied as a means of characterizing phytoplankton communities (IOCCG, 2014; Le Quéré et al., 2005; Nair et al., 2008). Phytoplankton cell size is considered a fundamental trait as it affects many important biological and ecological processes, including photosynthesis (Uitz et al., 2008), nutrient uptake (Raven, 1998), growth rate (Marañón, 2015), light absorption (Bricaud et al., 2004; Ciotti et al., 2002), carbon export (Guidi et al., 2009; Mouw et al., 2016), and the transfer of energy to higher trophic levels (Boyce et al., 2015). Thus, the size structure of phytoplankton assemblages can serve as a valuable indicator of the state of marine ecosystems and their response to environmental changes, including ocean warming (Marinov et al., 2010; Morán et al., 2010; Platt and Sathyendranath, 2008). Following the classification of Sieburth et al. (1978), phytoplankton are conventionally partitioned into three phytoplankton size classes (PSCs; see Table 1 for a list of symbols and

Table 1. Symbols and definitions.

Symbol	*Definition*	*Units*
a_d	absorption coefficient of non-algal particles	m^{-1}
a_{dg}	absorption coefficient of colored dissolved organic matter + non-algal particles	m^{-1}
a_g	absorption coefficient of colored dissolved organic matter	m^{-1}
[*Allo*]	alloxanthin concentration	mg m^{-3}
a_{ph}	absorption coefficient of phytoplankton	m^{-1}
a_{ph}^*	chorophyll-specific absorption coefficient of phytoplankton	m^2 mg^{-1}
[*But-fuco*]	19'-butanoyloxyfucoxanthin concentration	mg m^{-3}
[*Chl-a*]	chlorophyll-a concentration	mg m^{-3}
C_{DP}	chlorophyll-a concentration reconstructed from the weighted sum of diagnostic pigments	mg m^{-3}
C_{HPLC}	chlorophyll-a concentration measured by high-performance liquid chromatography	mg m^{-3}
C_{size}	chlorophyll-a concentration specific to size class "size"	mg m^{-3}
C^m_{size}	asymptotic maximum chlorophyll-a concentration of size class "size"	mg m^{-3}
D_{size}	fraction of size class "size" as total chlorophyll-a tends to zero	unitless
F_{size}	fraction of size class "size"	unitless
[*Fuco*]	fucoxanthin concentration	mg m^{-3}
GB	Georges Bank	–
GoM	Gulf of Maine	–
[*Hex-fuco*]	19'-hexanoyloxyfucoxanthin concentration	mg m^{-3}
MAB	Middle Atlantic Bight	–
MAD	mean absolute difference	unitless
NES	northeast U.S. continental shelf	–
[*Perid*]	peridinin concentration	mg m^{-3}
PSC	phytoplankton size class	–
r	Pearson correlation coefficient	unitless
R_{rs}	remote sensing reflectance	sr^{-1}
S	slope of a Type-II linear regression	unitless
SST	sea surface temperature	ºC
SFF	size-fractionated filtration	–
[*TAcc*]	total concentration of accessory pigments	mg m^{-3}
[*TChl-b*]	total chlorophyll-b concentration	mg m^{-3}
[*Zea*]	zeaxanthin concentration	mg m^{-3}
δ	bias	unitless

abbreviations used in this text): picoplankton (0.2-2 μm), nanoplankton (2-20 μm) and microplankton (20-200 μm).

A number of methods exist for quantifying PSCs *in situ*, including microscopy, size-fractionated filtration (SFF), conventional and imaging flow cytometry (Olson and Sosik, 2007), and high-performance liquid chromatography (HPLC) pigment analysis, each with their own advantages and limitations (IOCCG, 2014). While these methods are extremely useful, they can be labor-intensive, time consuming, and expensive, and as a result, the availability of *in situ* PSC data remains limited, thus limiting their use in studying and modeling large-scale, temporally dynamic ocean and ecosystem processes. Satellite remote sensing enables frequent, synoptic coverage of upper ocean optical properties and provides a means to characterize PSCs at spatial and temporal resolutions unattainable with *in situ* sampling. Given this fact, deriving information on phytoplankton size structure from satellite ocean color data is an active area of research, and a variety of algorithms have been developed for both global ocean (Brewin et al., 2015; Hirata et al., 2011) and regional applications (Brito et al., 2015; Di Cicco et al., 2017; Gittings et al., 2019; Sun et al., 2018, 2019a). Most current approaches for detecting PSCs from remote sensing can be categorized as either abundance-based or absorption-based, differing in terms of their theoretical frameworks and the remotely sensed parameters used as inputs (IOCCG, 2014; Mouw et al., 2017b).

Abundance-based algorithms exploit the generally observed co-variance of phytoplankton cell size and total biomass, indexed by its proxy, chlorophyll-a concentration ([*Chl-a*]; mg m^{-3}), to estimate the dominance or relative biomass fractions of PSCs (Brewin et al., 2010; Hirata et al., 2011; Uitz et al., 2006). For example, it is well

established that picoplankton, such as the cyanobacteria *Prochlorococcus and Synechococcus*, dominate in low-nutrient oligotrophic environments (e.g., central ocean gyres) and microplankton, including diatoms and dinoflagellates, comprise a greater fraction of total biomass in eutrophic, nutrient-rich regions (e.g., upwelling zones) (Chisholm et al., 1988; Margalef, 1978; Yentsch and Phinney, 1989). Abundance-based methods rely on empirical or semi-empirical relationships based on coincident *in situ* observations of size-fractionated [*Chl-a*], typically from HPLC pigments or SFF, and total [*Chl-a*] to model PSCs as a function of total [*Chl-a*]. Given that [*Chl-a*] is perhaps the most widely used and well-validated satellite ocean color product, abundance-based methods offer a straightforward, "user-friendly" approach for estimating PSCs from remote sensing. Yet, these methods are an indirect approximation of size structure, and the empirical relationships underlying them are subject to change both temporally and geographically, requiring ongoing assessment and re-calibration (Mouw et al., 2017b). Recent studies have demonstrated that the incorporation of additional environmental information attainable from remote sensing, such as sea surface temperature (*SST*), can improve the retrieval accuracy of abundance-based models (Brewin et al., 2017a; Moore and Brown, 2020; Ward, 2015).

Absorption-based algorithms distinguish PSCs directly from spectral variations in phytoplankton absorption ($a_{ph}(\lambda)$; λ denotes wavelength dependence), the amount of light absorbed by phytoplankton across the visible spectrum, which influences and can be derived from the reflectance signal measured by a satellite ocean color sensor (remote sensing reflectance ($R_{rs}(\lambda)$) (Ciotti and Bricaud, 2006; Devred et al., 2011; Mouw and Yoder, 2010). Larger cells are less efficient at absorbing light than smaller cells as a result

of pigment packaging, which results in a flattening of the chlorophyll-normalized phytoplankton absorption spectrum ($a_{ph}^{*}(\lambda)$) with increasing cell size, with the most pronounced change around 440 nm (Bricaud et al., 1988; Morel, 1987; Morel and Bricaud, 1981). Ciotti et al. (2002) demonstrated that despite physiological and taxonomic variability, cell size could explain >80% of the variance in $a_{ph}^{*}(\lambda)$ spectral shape over the wavelength range 400-700 nm. An advantage of absorption-based methods over abundance-based approaches is that they can detect changes in PSCs that do not co-vary with total [*Chl-a*] (e.g., blooms of smaller cells). Moreover, as absorption-based methods are based on a direct optical response rather than indirect empirical relationships, they are less likely to require re-calibration over time or for different ocean regions. However, the limited spectral resolution of current multi-spectral ocean color instruments and inherent ambiguity in the optical signals of in-water constituents can make retrieving accurate $a_{ph}(\lambda)$ spectral shape and magnitude challenging. This is particularly true in optically complex coastal and continental shelf waters with high concentrations of colored dissolved organic matter (CDOM) and non-algal particles (NAP), which overlap with phytoplankton in their contribution to the total light absorption in the blue region of the spectra, where satellite retrievals are subject to large uncertainties related to atmospheric correction and issues with sky and sun glint (Estrella et al., 2020).

Given the unique strengths and limitations of these different satellite PSC algorithm approaches, evaluating their performance in different ocean regions and whether they may be optimized for regional application is essential. Several studies have successfully retrieved PSCs at regional scales, including the Red Sea (Gittings et al., 2019), the

Mediterranean Sea (Di Cicco et al., 2017), the Western Iberian coast (Brito et al., 2015), and the continental shelf seas of China (Sun et al., 2018, 2019a) through re-parameterization of global abundance-based models with local *in situ* data sets. These studies demonstrate the potential for PSC model optimization in other ocean regions, which may provide benefits for regional-scale applications, including food web modeling and ecosystem-based fisheries management.

The northeast U.S. continental shelf (NES) is a highly productive, temperate marine ecosystem that supports many commercially and recreationally important fisheries (Hare et al., 2016; National Marine Fisheries Service, 2018). The NES is physically dynamic and optically complex (Mannino et al., 2014; Pan et al., 2008), thus necessitating evaluation and potential optimization of existing PSC algorithms to ensure their accuracy. Phytoplankton species composition and biomass in the NES vary seasonally, with diatoms dominating in a typical winter-spring bloom and other taxa, such as cryptophytes and cyanobacteria, becoming more prevalent during the summer (O'Reilly and Zetlin, 1998; Pan et al., 2011; Richaud et al., 2016).

In this study, we aim to evaluate and optimize several existing abundance-based and absorption-based PSC algorithms for application to ocean color imagery in the NES region, with the goal of improving PSC imagery products for long-term time series investigations and integration into regional ecosystem and fisheries modeling efforts. Primarily, we address the following questions:

- To what extent does regional re-parameterization using a local *in situ* data set improve the performance of abundance-based PSC models in the NES?

- Does incorporating *SST* into an abundance-based model improve PSC retrieval accuracy in the NES?
- How do abundance-based and absorption-based algorithms compare in their estimations of PSCs in the NES?

2. Data and methods

2.1 Study area

The NES region (35ºN-45.5ºN, 64ºW-77ºW) extends along the east coast of the U.S. from Cape Hatteras, NC, USA to Nova Scotia, Canada (Fig. 1). The region includes three primary subregions: the Mid-Atlantic Bight (MAB; 36ºN-41ºN, 70ºW-76ºW), Georges Bank (GB; 40ºN-42ºN, 66ºW-70ºW), and the Gulf of Maine (GoM; 42ºN-45ºN, 66ºW-71ºW). The shelf is commonly defined as inshore of the 200 m isobath, with deeper basins in the GoM exceeding 300 m depth. The NES is influenced by two major current systems: the warm, saline, northward flowing Gulf Stream, and the colder, fresher, southward flowing Labrador Current. Mesoscale features (e.g., eddies, fronts) and interannual variations in the path and flow of these two currents affect nutrient fluxes, productivity, and phytoplankton community composition across the region (Saba et al., 2015; Schollaert et al., 2004). The NES has experienced rapid warming in recent decades (Pershing et al., 2015), which has been connected to changes in phytoplankton bloom dynamics (Hunter-Cevera et al., 2016) and the distributions of fish and other marine species (Friedland et al., 2020; Kleisner et al., 2017). The NES is a well-studied region relative to other parts of the global ocean, with routine oceanographic surveys conducted throughout the region since the late 1970s (O'Reilly and Zetlin, 1998). At present, NOAA's

Northeast Fisheries Science center Ecosystem Monitoring (EcoMon) program provides a range of hydrographic and biological data for the region (National Marine Fisheries Service, 2020).

2.2 In situ data

Discrete surface (upper 10 m) samples of HPLC pigments and the spectral absorption of phytoplankton ($a_{ph}(\lambda)$), CDOM ($a_g(\lambda)$), and NAP ($a_d(\lambda)$) collected throughout the NES region from 2003 to 2018 were acquired from NASA's SeaWiFS Bio-optical Archive and Storage System (SeaBASS; https://seabass.gsfc.nasa.gov/) (Fig. 1). The compiled data were from several different cruises and experiments, with the largest portion from the Impacts of Climate Variability on Primary Production and Carbon Distributions in the Middle Atlantic Bight and Gulf of Maine (CliVEC) field campaign (Mannino et al., 2009) and the University of New Hampshire Western Gulf of Maine time series (Moore, 2006) (Table 2). Only HPLC pigment samples with a full set of seven diagnostic pigments required for estimating PSCs (fucoxanthin, peridinin, 19'-hexanoyloxyfucoxanthin, 19'-butanoyloxyfucoxanthin, alloxanthin, total chlorophyll-b, and zeaxanthin) were included in this analysis (see Section 2.6). For the absorption data, only measurements with 1-nm spectral resolution over the range 400-700 nm with coincident HPLC pigment measurements were retained. In order to calculate the combined absorption of CDOM and NAP ($a_{dg}(\lambda)$), a parameter routinely retrieved by satellite inversion algorithms, measurements of $a_g(\lambda)$ without matching $a_d(\lambda)$ (and vice-versa) were excluded. For stations with multiple samples in the upper 10 m, the data were averaged. To limit the effects of very shallow water and near-coastal processes, stations with a depth <25 m were removed prior to analysis.

In addition to the data obtained from SeaBASS, 40 HPLC, 24 $a_{ph}(\lambda)$, and 14 $a_g(\lambda)/a_d(\lambda)$ samples collected by our group on the Summer 2018 and Fall 2018 NOAA EcoMon surveys were also included. HPLC samples from these cruises were collected according to the NASA Ocean Optics Protocols (Mueller et al., 2003) and analyzed at Horn Point Laboratory (University of Maryland Center for Environmental Science). Absorption measurements were collected and analyzed following the procedures detailed in Mouw et al. (2017a).

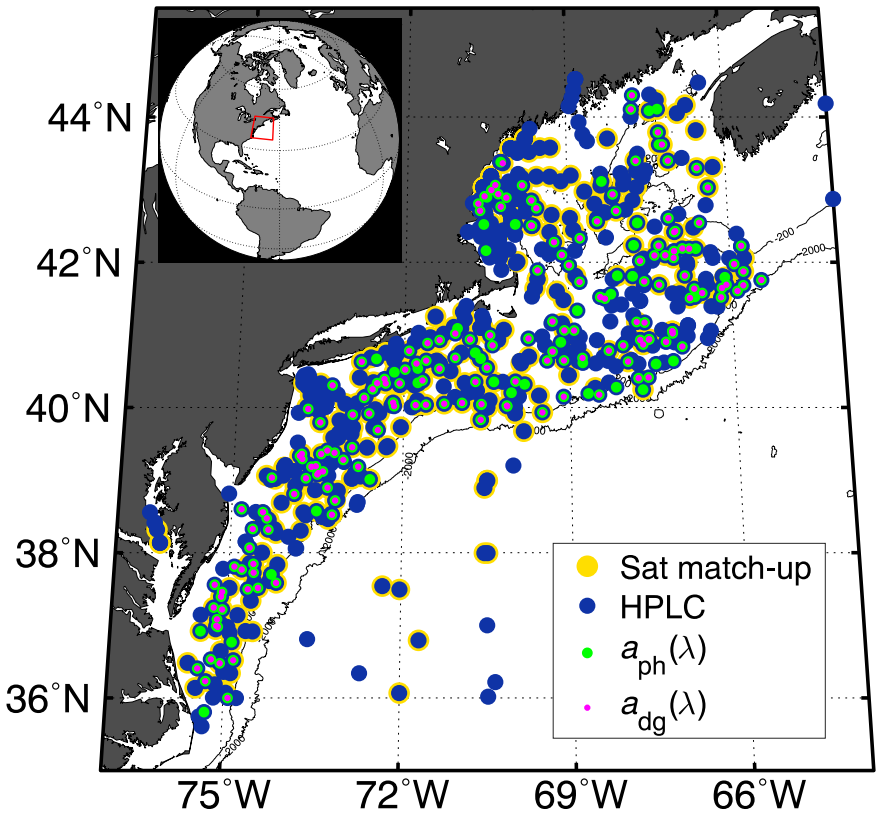

Figure 1 Locations of the in situ data and satellite match-ups used in this study. The 200 and 2000 m isobaths from the 2019 General Bathymetric Chart of the Oceans (https://www.gebco.net/) are shown for reference. See Table 2 for information on data sources.

Table 2. Summary of *in situ* data sources. *N* denotes the number of samples (after QA) and the number in parentheses refers to the number of satellite match-ups. Citations for the individual data sets from SeaBASS are also provided.

Cruise/Experiment - P.I.(s)	*Years(s)*	*Month(s)*	*N, HPLC*	*N,* $a_{ph}()$	*N,* $a_{dg}()$
Impacts of Climate Variability on Primary Production and Carbon					
NOAA Ecosystem Monitoring (EcoMon) - Mannino et al., 2013	2013, 2018	Feb, Aug, Nov	71 (41)	24 (18)	14 (9)
Tara Oceans Expedition - Boss et al., 2009	2012	Jan, Feb	2	0	0
LOBO timeseries - Roesler, 2009	2009	Mar	6	0	0
Ocean Color Cal Val (OCV) - Hooker et al., 2005	2007, 2009	May, Nov	16 (7)	0	0
Delaware and Chesapeake Bay Fluorescence - Chekalyuk, 2008	2008	May	1	0	0
BIOCOMPLEXITY - Harding, 2001	2003	Aug	2 (1)	0	0
		Totals:	786 (368)	214 (123)	173 (99)

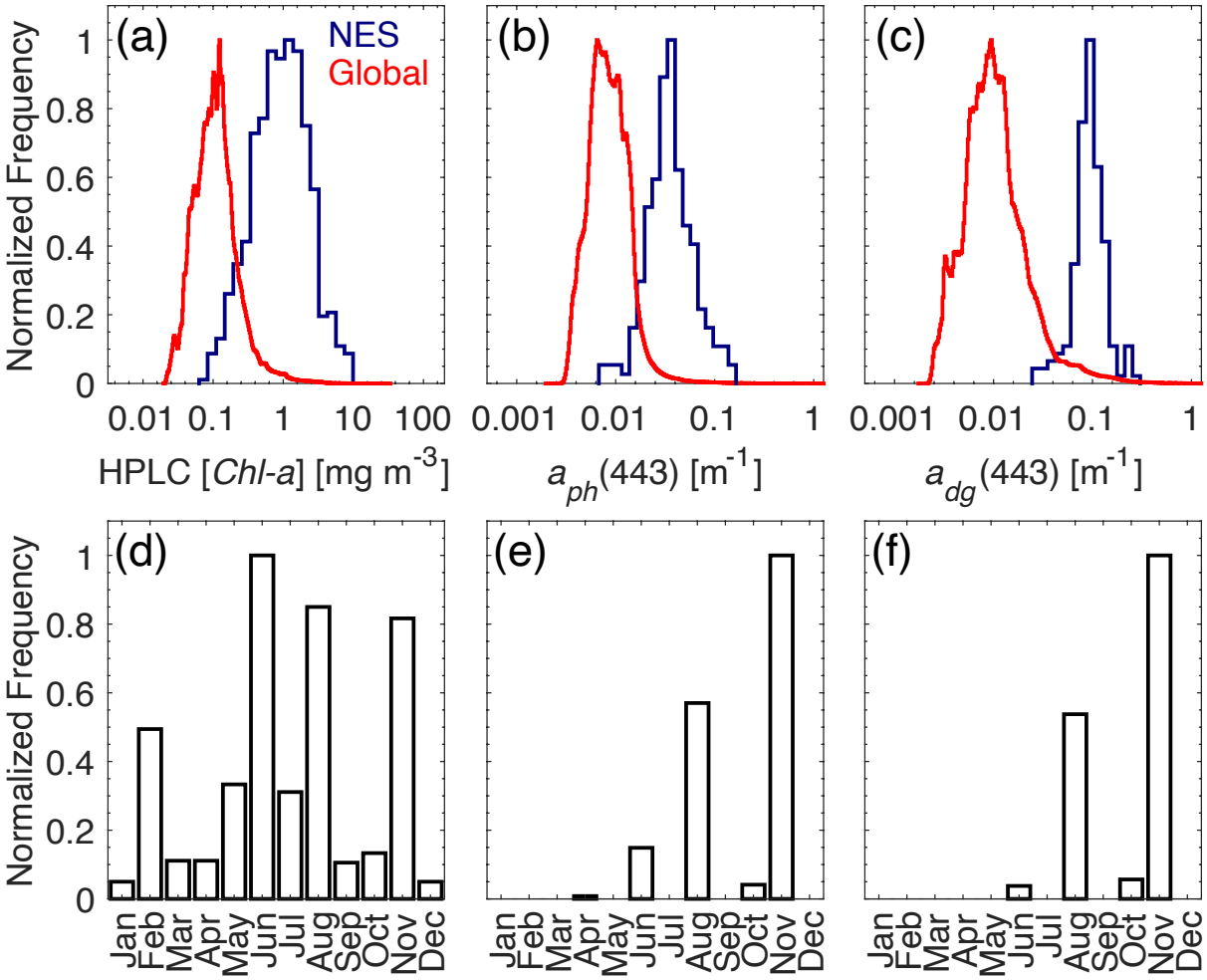

Figure 2. Relative frequencies of in situ observations from the NES data set used in this study (blue stairs): (a) HPLC-measured [Chl-a] (N = 786), (b) aph(443) (N = 214) and (c) adg(443) (N = 173), with their respective monthly distributions (d-f, black black bars). Global distributions from an OC-CCI v4.2 annual satellite composite for 2018 are overlaid for comparison (red line). Frequencies were normalized by the maximum value.

Quality assurance (QA) for the HPLC pigment data was carried out following Uitz et al. (2006). First, to account for differences in the detection limits and sensitivities of different HPLC processing methods, pigment concentrations <0.001 mg m^{-3} were set to zero. Then, utilizing the relationship of Trees et al. (2000), who demonstrated that [*Chl-a*] and the total concentration of major accessory pigments ([*TAcc*]) co-vary in log-linear fashion within the euphotic zone of diverse oceanic regions, a robust linear regression (MATLAB function *robustfit.m*) of [*TAcc*] on [*Chl-a*] was performed to identify outliers. Any points exceeding three standard deviations with respect to the mean co-variation were

excluded. QA for the $a_{ph}(\lambda)$, $a_g(\lambda)$, and $a_d(\lambda)$ data consisted of the following steps: (1) overly noisy spectra were manually identified and removed; (2) spectra with negative values not exceeding -0.1 were offset by the most negative value (Grunert et al., 2019); (3) spectra were smoothed using a Savitsky-Golay filtering technique (MATLAB function *sgolayfilt.m*) with a 9-nm smoothing window (Torrecilla et al., 2011). The $a_g(\lambda)$ and $a_d(\lambda)$ values were then summed to obtain $a_{dg}(\lambda)$. After QA, a total of 786 HPLC, 214 $a_{ph}(\lambda)$, and 173 $a_{dg}(\lambda)$ measurements remained. The pigment data were representative of every month of the year, with a slight bias towards summer months, whereas $a_{ph}(\lambda)$ and $a_{dg}(\lambda)$ data were almost exclusively limited to summer and fall months (Fig. 2).

2.3 Satellite data

Daily, Level-3 mapped (4-km resolution, sinusoidal projected) estimates of $R_{rs}(\lambda)$, [*Chl-a*], $a_{ph}(\lambda)$, and $a_{dg}(\lambda)$ from the most recent version of the European Space Agency's (ESA) Ocean Colour – Climate Change Initiative product (OC-CCI v4.2; Sathyendranath et al., 2019) at the time of the initiation of this study were downloaded from https://esa-oceancolour-cci.org/. OC-CCI v4.2 consists of merged, bias-corrected data from the Sea-viewing Wide-Field-of-View Sensor (SeaWiFS), Medium Resolution Imaging Spectrometer (MERIS), Moderate Resolution Imaging Spectroradiometer (MODIS-Aqua), and Visible Infrared Imaging Radiometer Suite (VIIRS-SNPP) satellite sensors over the period 1997-2019. The multi-sensor data are band-shifted to SeaWiFS reference wavelengths (412, 443, 490, 510, 555, and 670 nm) and include per-pixel uncertainty estimates. OC-CCI v4.2 also incorporates the latest NASA re-processing (R2018), which corrected for significant drift in the MODIS-Aqua sensor. The reader is referred to the OC-

CCI v4.2 Product User Guide (https://esa-oceancolour-cci.org/documents-list) for a more detailed overview.

The standard OC-CCI [*Chl-a*] algorithm uses a blended combination of NASA's OC3, OCI, and OC5 algorithms (Gohin et al., 2002; Hu et al., 2012; O'Reilly et al., 1998) based on optical water classes (Jackson et al., 2017; Moore et al., 2009), which improves performance in optically complex waters. In addition to the standard algorithm, we also calculated [*Chl-a*] using the regional algorithm of Pan et al. (2010). This regional empirical algorithm was developed using coincident *in situ* measurements of HPLC pigments and $R_{rs}(\lambda)$ collected at various locations across the MAB and GoM and was applied using the published coefficients for SeaWiFS wavebands. The standard OC-CCI $a_{ph}(\lambda)$ and $a_{dg}(\lambda)$ products, derived using the Quasi-Analytical Algorithm (QAA_v5) of Lee et al. (2009), were used in this study.

For validation of the satellite input products ([*Chl-a*], $a_{ph}(\lambda)$, and $a_{dg}(\lambda)$) and PSC algorithm output, *in situ* samples were matched in time and space with the satellite data. Following convention, match-ups were determined as the geometric median of a 3x3 pixel box centered on the sampling location (nearest latitude and longitude), and only match-ups with at least 5 valid pixels and a median coefficient of variation of <0.15 for $R_{rs}(\lambda)$ bands between 412 and 555 nm were used to ensure spatial homogeneity (Bailey and Werdell, 2006). As OC-CCI is a daily, multi-sensor product, a same-day coincidence window was used rather than the more stringent ±3-hour window recommended for a single mission by Bailey and Werdell (2006). This resulted in 368 [*Chl-a*], 123 $a_{ph}(\lambda)$, and 99 $a_{dg}(\lambda)$ match-ups (Table 2). Furthermore, all *in situ* pigment samples were matched with daily estimates of *SST* from the Multi-scale Ultra-high Resolution *SST* analysis (MUR

v4.1) (Chin et al., 2017). MUR is a gap-filled, 1-km resolution gridded global *SST* product that combines night-time infrared SST retrievals from the MODIS sensor with multiple other in-orbit infrared/microwave instruments and data from NOAA's in situ *SST* Quality Monitor (iQuam) database (Xu and Ignatov, 2014). Data for the period June 1, 2002 - December 31, 2019 were downloaded freely from NASA's Physical Oceanography Distributed Active Archive Center (PO.DAAC; https://podaac.jpl.nasa.gov).

2.4 Data partitioning for model re-parameterization and validation

To allow for both the re-parameterization of abundance-based PSC models (see Sections 2.7.1.6 and 2.7.1.7) and independent model validation, the pigment data were split into two separate data sets. Of the 786 total samples, the 368 samples with a valid satellite [*Chl-a*] match-up (47% of the data) were removed and reserved for independent validation and are referred to as the validation data set. The remainder of the data (N = 418) were used for model re-parameterization and are referred to as the parameterization data set.

2.5 Statistical metrics

We used several statistical metrics to compare algorithm estimates with the *in situ* data and evaluate algorithm performance. To measure accuracy, we used the mean absolute difference (*MAD*). While many studies commonly consider the root mean square difference (*RMSD*), *MAD* has been recommended as a more unambiguous and appropriate metric for model assessment (Seegers et al., 2018; Willmott and Matsuura, 2005). To measure systematic bias, we used the mean bias (δ). The *MAD* and δ are calculated according to:

$$MAD = \frac{1}{N}\sum_{i=1}^{N}|M_i - O_i| \quad (1)$$

and

$$\delta = \frac{1}{N}\sum_{i=1}^{N}(M_i - O_i), \quad (2)$$

where *M*, *O*, and *N* represent the modeled value (i.e., satellite estimate), the observed value (i.e., *in situ*), and the number of samples, respectively. A positive (negative) δ indicates a model's tendency to systematically overestimate (underestimate) the variable of interest. We also computed the Pearson correlation coefficient (*r*) and slope of a Type-II linear regression (*S*) for additional comparison between modeled and *in situ* values (Brewin et al., 2015b; Werdell et al., 2013). Type-II regression (MATLAB function *lsqfitgm.m*) was applied rather than Type-I regression as it accounts for the inherent measurement uncertainties of *in situ* field data (Laws and Archie, 1981). While values of *r* and *S* that are close to one generally indicate better agreement between model estimates and *in situ* observations, *r* and *S* alone provide no information on the accuracy or bias of a given model, and thus are not viewed in isolation from the *MAD* and δ when assessing model performance. Statistical calculations involving total or size-specific [*Chl-a*], $a_{ph}(\lambda)$, or $a_{dg}(\lambda)$ were performed in $\log_{10}$ space, while calculations involving size fractions were performed in linear space.

2.6 Estimation of PSCs from HPLC pigments

For algorithm re-parameterization and validation, PSCs were estimated from the pigment data using the Diagnostic Pigment Analysis (DPA) method (Brewin et al., 2015a; Claustre, 2005; Devred et al., 2011; Uitz et al., 2006; Vidussi et al., 2001). This method has been used extensively for PSC algorithm development and validation given the

relative abundance of HPLC pigment measurements compared with other *in situ* PSC methods. The DPA approach involves first re-constructing the measured [*Chl-a*] (denoted here as C_{HPLC}) from the weighted sum of seven biomarker pigments (denoted C_{DP}) according to:

$$C_{DP} = \sum_{i=1}^{7} W_i \, P_i, \quad (3)$$

where [***W***] represents pigment-specific weighting coefficients and [***P***] is the set of seven biomarker pigments: {fucoxanthin ([*Fuco*]), peridinin ([*Perid*]), 19'-hexanoyloxyfucoxanthin ([*Hex-fuco*]), 19'-butanoyloxyfucoxanthin ([*But-fuco*]), alloxanthin ([*Allo*]), total chlorophyll-b ([*TChl-b*]), zeaxanthin ([*Zea*])}. To derive an optimal set of weighting coefficients from the NES pigment data set, a multi-linear regression of [***P***] on C_{HPLC} was performed. The newly computed weighting coefficients compared reasonably with those obtained from previous studies (Table 3), with the exception of large differences observed for the weights attributed to [*But-fuco*] and [*Allo*], which may be due to differences in community composition in the NES compared with the global ocean. The new weights yielded close agreement between C_{DP} and C_{HPLC} (*MAD* = 0.12, r = 0.98), and demonstrated better results relative to using the unweighted sum of the diagnostic pigments (Vidussi et al., 2001), or the commonly applied weights of Uitz et al. (2006), which were derived from a large global pigment database (Fig. 3, Table 3).

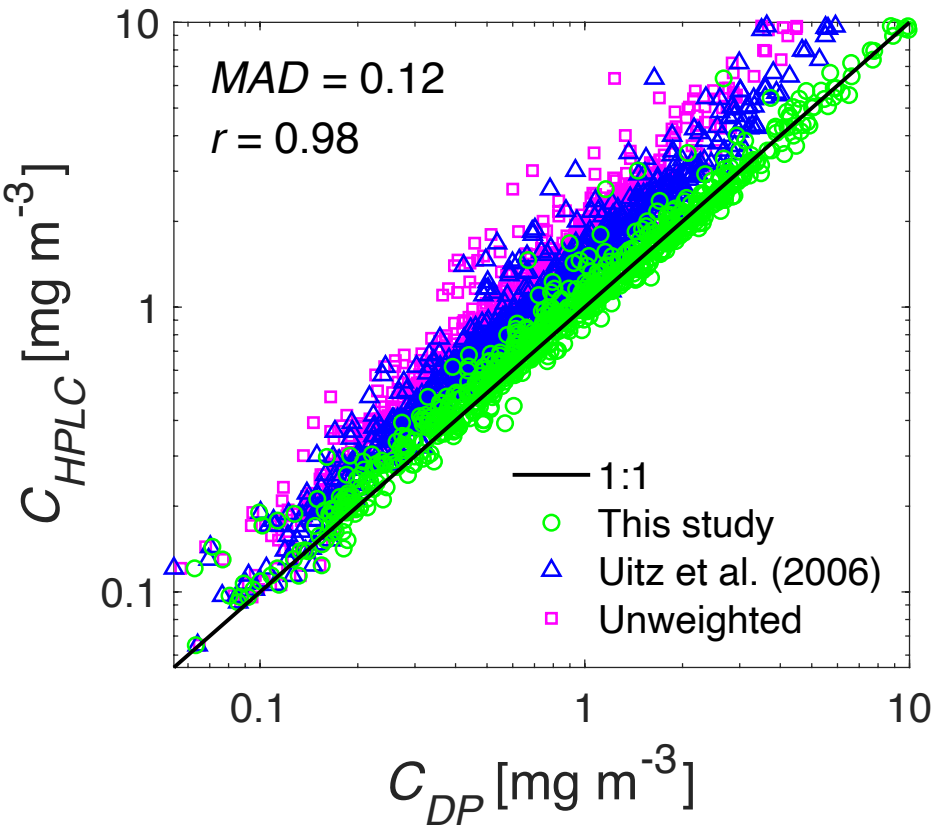

*Figure 3 Comparison of the HPLC-measured [*Chl-a*] (C_{HPLC}) and the reconstructed [*Chl-a*] from the sum of seven diagnostic pigments (C_{DP}) using the weighting coefficients derived from this study (green circles;* MAD = *0.12,* r = *0.98), the weights derived by Uitz et al. (2006) from a global data set (blue triangles;* MAD = *0.47,* r = *0.96), and no weighting coefficients (magenta squares;* MAD = *0.62,* r = *0.96).*

The fractional contributions of micro-, nano-, and picoplankton were estimated from the ratios of the diagnostic pigments attributed to each size class to C_{DP}. Two

Table 3. Diagnostic pigments [***P***] and their associated taxonomic groups and attributed size classes, along with weighting coefficients [***W***] obtained from this study and previous studies. The number of data points and geographical regions of each study are also provided.

*Pigment [**P**]*	*Primary taxonomic group(s)*	*Attributed size class(es)*	*Weights [**W**]*			
			This study	*Uitz et al. (2006)*	*Brewin et al. (2015a)*	*Brewin et al. (2017)*
Fucoxanthin (P_1)	Diatoms	Micro/nano	2.20	1.41	1.51	1.65

Peridinin (P_2)	Dinoflagellates	Micro	1.08	1.41	1.35	1.04
19'-Hex (P_3)	Prymnesiophytes	Nano	0.86	1.27	0.95	0.78
19'-But (P_4)	Pelagophytes	Nano	3.63	0.35	0.85	1.19
Alloxanthin (P_5)	Cryptophytes	Nano	-0.10	0.60	2.71	3.14
Total chlorophyll-b (P_6)	Prochlorophytes, Chlorophytes	Pico	1.21	1.01	1.27	1.38
Zeaxanthin (P_7)	Prochlorophytes, Cyanobacteria	Pico	0.99	0.86	0.93	1.02
		Number of data points	786	2419	5841	2239
		Geographic region	NES	Global	Global	North Atlantic

diagnostic pigments were attributed to microplankton: [*Fuco*] and [*Perid*], associated with diatoms and dinoflagellates, respectively. Acknowledging that [*Fuco*] is also present in prymnesiophytes and chrysophytes, and that diatoms can also occupy the nano size range, Devred et al. (2011) introduced a modification that attributes a portion of [*Fuco*] (P_1) to nanoplankton, such that $P_1 = P_{1,nano} + P_{1,micro}$. In their approach, $P_{1,nano}$ is estimated from the equation:

$$P_{1,nano} = 10^{[q_1 log_{10}(P_3) + q_2 log_{10}(P_4)]}, \quad (4)$$

where P_3 and P_4 are the pigments [*Hex-fuco*] and [*But-fuco*], respectively, and q_1 and q_2 are the coefficients of a 1% multi-linear quantile regression of P_1 on P_3 and P_4. Following the same approach, The coefficients q_1 and q_2 were re-computed for the NES pigment dataset, obtaining values of q_1 = 0.999 and q_2 = 0.271, and $P_{1,nano}$ was estimated using Eq. (4). In any instance where the estimated $P_{1,nano}$ was found to be greater than P_1, it was set equal to P_1. The fraction of microplankton (F_{micro}) was then calculated according to:

$$F_{micro} = \frac{\sum_{i=1}^{2} W_i \, P_i - W_1 P_{1,nano}}{C_{DP}}. \quad (5)$$

Three diagnostic pigments were used to estimate nanoplankton: [*Hex-fuco*], [*But-fuco*], and [*Allo*], attributed to prymnesiophytes, pelagophytes, and cryptophytes, respectively (Brewin et al., 2015a; Roy, 2011; Uitz et al., 2006). Brewin et al. (2010) proposed a linear adjustment that attributes a portion of [*Hex-fuco*] to picoeukaryotes (picoplankton) in ultra-oligotrophic environments ([*Chl-a*] < 0.08 mg m^{-3}). However, considering that only one sample in the data set used in this study met this criterion ([*Chl-a*] = 0.07 mg m^{-3}) and the adjustment was found to make only minor difference (not shown), it was excluded for simplicity. Incorporating the [*Fuco*] modification of Devred et al. (2011), the fraction of nanoplankton was calculated as:

$$F_{nano} = \frac{\sum_{i=3}^{5} W_i \, P_i + W_1 P_{1,nano}}{C_{DP}}. \quad (6)$$

The final two diagnostic pigments: [*TChl-b*] and [*Zea*], were attributed to the picoplankton class, the former associated with prochlorophytes and chlorophytes and the latter with prochlorophytes and cyanobacteria (Chisholm et al., 1988; Roy, 2011; Uitz et al., 2006). The fraction of picoplankton (F_{pico}) was computed as:

$$F_{pico} = \frac{\sum_{i=6}^{7} W_i \, P_i}{C_{DP}}. \quad (7)$$

Once F_{micro}, F_{nano}, and F_{pico} (collectively referred to as F_{size}) were determined, the [*Chl-a*] specific to each size class (collectively referred to as C_{size}) was calculated by multiplying F_{size} by C_{HPLC}, such that:

$$C_{micro} = F_{micro} C_{HPLC}, \quad (8a)$$

$$C_{nano} = F_{nano} C_{HPLC}, \quad (8b)$$

$$C_{pico} = F_{pico} C_{HPLC}. \quad (8c)$$

2.7 PSC algorithms

A variety of PSC algorithms, including purely abundance-based methods, abundance-based methods that include *SST*, and absorption-based approaches, were selected for optimization and/or evaluation in this study. The abundance-based models chosen are among the most commonly applied in the literature and have been successfully re-parameterized for studies in diverse ocean regions, including continental shelf systems (Brito et al., 2015; Sun et al., 2018). The absorption-based models were chosen based on their global performance metrics (Mouw et al., 2017b) and their demonstrated consistency in capturing multiple phytoplankton phenology metrics in the North Atlantic (Kostadinov et al., 2017). The following sections provide brief overviews of each model, including their principal frameworks, methods used for model development/parameterization, and key differences. For more comprehensive information, the reader is referred to the original publications and the reviews of Mouw et al. (2017b) and IOCCG (2014).

2.7.1 Abundance-based

2.7.1.1 Brewin et al. (2010, 2015a)

The three-component model of Brewin et al. (2010) relates the fractional contribution of combined pico- and nanoplankton ($F_{pico,nano}$) and picoplankton (F_{pico}) to [*Chl-a*] using two exponential functions (Sathyendranath et al., 2001) according to:

$$F_{pico,nano} = \frac{C^m_{pico,nano}\left[1 - exp\left(-\frac{D_{pico,nano}}{C^m_{pico,nano}}[Chl\text{-}a]\right)\right]}{[Chl\text{-}a]}, \quad (9)$$

$$F_{pico} = \frac{C_{pico}^{m}\left[1 - exp\left(-\frac{D_{pico}}{C_{pico}^{m}}[Chl\text{-}a]\right)\right]}{[Chl\text{-}a]}, \quad (10)$$

where the model parameters $C^m_{pico,nano}$ and C^m_{pico} represent asymptotic maximum [*Chl-a*] for the associated size classes, and $D_{pico,nano}$ and D_{pico} represent the fraction of each size class as [*Chl-a*] tends toward zero. The model parameters are derived by fitting Eqs. 9 and 10 to an *in situ* data set of $F_{pico,nano}$, F_{pico}, and [*Chl-a*] via nonlinear least squares regression. F_{micro} and F_{nano} are then determined as $F_{micro} = 1 - F_{pico,nano}$ and $F_{nano} = F_{pico,nano} - F_{pico}$, respectively. Brewin et al. (2010) used a data set of HPLC pigments from the Atlantic Ocean (*N* = 1935) (Atlantic Meridional Transect cruises 5-15) and estimated PSCs using DPA to derive model parameters. Brewin et al. (2015a) utilized a much larger global data set of HPLC measurements (*N* = 5841) to compute the model parameters. These two models are denoted B10 and B15 throughout the remainder of the text. For simplicity, the notation B10 is also used to refer to the general framework that underlies both models (i.e., Eqs. 9 and 10), in addition to the parameterization specific to that study. Further, while Brewin et al. (2015a) also investigated the influence of average irradiance in the mixed layer on model parameters, in this study B15 refers to the model without this modification. Parameter values obtained from various studies are provided in Table 4.

2.7.1.2 Brewin et al. (2017)

Brewin et al. (2017) used a merged *in situ* HPLC/SFF data set from the North Atlantic (*N* = 2239) to compute the parameters of the B10 model (Eqs. 9 and 10). They then modified the model parameters to vary as a function of *SST* by matching the *in situ* PSC data with satellite-derived *SST* and conducting a running fit of the model to the data

binned by increasing *SST*. They represented the resulting relationships between *SST* and model parameters using logistic functions, such that $C^m_{pico,nano}$, C^m_{pico}, $D_{pico,nano}$ and D_{pico} are expressed as:

$$C^m_{pico,nano} = 1 - \{\frac{G_1}{1 + \exp\left[-G_2(SST - G_3)\right]} + G_4\}, \quad (11)$$

$$C^m_{pico} = 1 - \{\frac{H_1}{1 + \exp\left[-H_2(SST - H_3)\right]} + H_4\}, \quad (12)$$

$$D_{pico,nano} = \frac{J_1}{1 + \exp\left[-J_2(SST - J_3)\right]} + J_4, \quad (13)$$

$$D_{pico} = \frac{K_1}{1 + \exp\left[-K_2(SST - K_3)\right]} + K_4, \quad (14)$$

where G_i, H_i, J_i, and K_i (where i = 1-4) are empirical parameters controlling the shape of the respective logistic curve and are provided in Table 4 of Brewin et al. (2017). In the remainder of this text, the notation B17 is used to refer to the *SST*-independent parameterization of the model, which uses a single set of model parameters derived from their full data set (Table 4). The *SST*-dependent parameterization, which uses Equations 11-14 with the published coefficients, is denoted as B17-*SST*.

2.7.1.3 Devred et al. (2011)

The model of Devred et al. (2011) (denoted D11) is based on the same exponential functions as the B10 model (Eqs. 9 and 10). The primary difference is that the model parameters $C^m_{pico,nano}$ and C^m_{pico} were not derived from HPLC pigment-based size classes, but rather by successive application of the two-population absorption model of Devred et al. (2006) to $a_{ph}(\lambda)$ and [*Chl-a*] data from the Northwest Atlantic and NASA's NOMAD data set. While the model was originally applied as a spectral-based approach, in this study it is implemented as an abundance-based method, using the parameters

provided in Table 2 of Brewin et al. (2015a). In a comparison of nine existing PSC algorithms in the Northwest Atlantic region near Newfoundland, Liu et al. (2018) found the application of this model as an abundance-based method to be the most successful (Model E in their study). The reader is referred to Chapter 4 of IOCCG (2014) for more information on this approach.

2.7.1.4 Hirata et al. (2011)

The empirical model of Hirata et al. (2011) (denoted H11) estimates the fractional contribution of pico- and microplankton to [*Chl-a*] according to:

$$F_{pico} = -[a_1 + exp(a_2X + a_3)]^{-1} + a_4X + a_5\,, \quad (15)$$

$$F_{micro} = [b_1 + exp(b_2X + b_3)]^{-1}\,, \quad (16)$$

where a_i and b_i (where i = 1-5 and i = 1-3, respectively) are empirical coefficients specific to each size class and X is log10-transformed [*Chl-a*]. F_{nano} is then calculated by difference ($1 - F_{micro} - F_{pico}$). The H11 model was developed using PSCs derived from a global HPLC data set (N = 2776) following a unique version of DPA that attributes [*TChl-b*] to nanoplankton rather than picoplankton, as in Brewin et al. (2010, 2015a, 2017) and the present study (see Section 2.6).

2.7.1.5 Moore and Brown (2020)

The model of Moore and Brown (2020) utilizes the H11 microplankton model (Eq. 16) to estimate both F_{pico} and F_{micro}. Using a data set of surface HPLC pigments from the Atlantic Ocean (N = 1083), they developed two separate models: one parameterized using the DPA method (following the procedure of Brewin et al. (2015a)) and one parameterized using CHEMTAX (Mackey et al., 1996). They then incorporated different remotely sensed environmental variables into the models, following a similar approach to

that of Brewin et al. (2015a, 2017), and created a look-up table (LUT) for each model parameter indexed by the environmental data. Of the environmental variables tested, they found that the inclusion of *SST* resulted in the largest reduction of model error. In this study, the DPA version of the model was applied, both with and without the incorporation of *SST*. The *SST*-independent model (denoted MB20) was applied using Eq. (16) with the coefficients provided in Table 4 of Moore and Brown (2020). The *SST*-dependent model (denoted MB20-*SST*) was applied using the set of parameters from their LUT indexed by *SST* (obtained from Timothy Moore via personal communication).

2.7.1.6 Re-parameterized B10 and H11 models

We derived new model parameters for the B10 and H11 models using the pigment-based estimates of F_{size} from the NES parameterization data set (Table 3). To re-parameterize the B10 model, Eqs. (9) and (10) were fit to $F_{pico,nano}$, F_{pico}, and C_{HPLC} using a standard nonlinear least squares curve fitting method (MATLAB function *lsqcurvefit.m*, Levenberg-Marquardt algorithm) (Brewin et al., 2017; Brewin et al., 2015a). We followed the same procedure for the H11 model, however with a slight modification. Considering the findings of Moore and Brown (2020), who showed better results when using the H11 microplankton formula (Eq. 16) for estimating both F_{micro} and F_{pico}, we tested the fit of both Eq. (15) and Eq. (16) to our data set of F_{pico} and C_{HPLC}. We likewise found improved fit statistics when using Eq. (16) to estimate F_{pico} (not shown). Therefore, we fit Eq. (16) to both F_{micro} and F_{pico} and C_{HPLC} to derive new model parameters. We refer to these two regionally re-parameterized abundance-based models as B-NES and H-NES, respectively.

Table 4. Parameter values for the abundance-based models of Brewin et al. (2010) (Eqs. 9 and 10) and Hirata et al. (2011) (Eq. 16), obtained from this study and from previous studies.

Study	*Geographic region*	*Years*	*Parameters for Equations (9) and (10)*					
				$C^m_{pico,nano}$	C^m_{pico}	$D_{pico,nano}$	D_{pico}	
Brewin et al. (2010)	Atlantic	1997-2004	-	1.06	0.11	0.9	0.73	-
Brewin et al. (2015a)	Global	1992-2012	-	0.77	0.13	0.94	0.91	-
Brewin et al. (2017)	N Atlantic	1995-2015	-	0.82	0.13	0.87	0.73	-
Devred et al. (2011)	NW Atlantic	1996-2003	-	0.55	0.15	1.00	1.00	-
This study	NES	2003-2018	-	0.81	0.15	0.78	0.54	-
			Parameters for Equation (16)					
			$b_{1,micro}$	$b_{2,micro}$	$b_{3,micro}$	$b_{1,pico}$	$b_{2,pico}$	$b_{3,pico}$
Hirata et al. (2011)	Global	1995-2008	0.91	-2.73	0.40	-	-	-
Moore and Brown (2020)	Atlantic	1997-2014	0.82	-1.33	0.39	1.41	2.62	1.72
This study	NES	2003-2018	1.03	-1.68	-0.12	-3.45	0.67	2.29

2.7.1.7 Regional SST-modified B10 model

Following a similar methodology to recent studies (Brewin et al., 2019, 2017; Moore and Brown, 2020; Sun et al., 2019), we investigated the influence of *SST* on

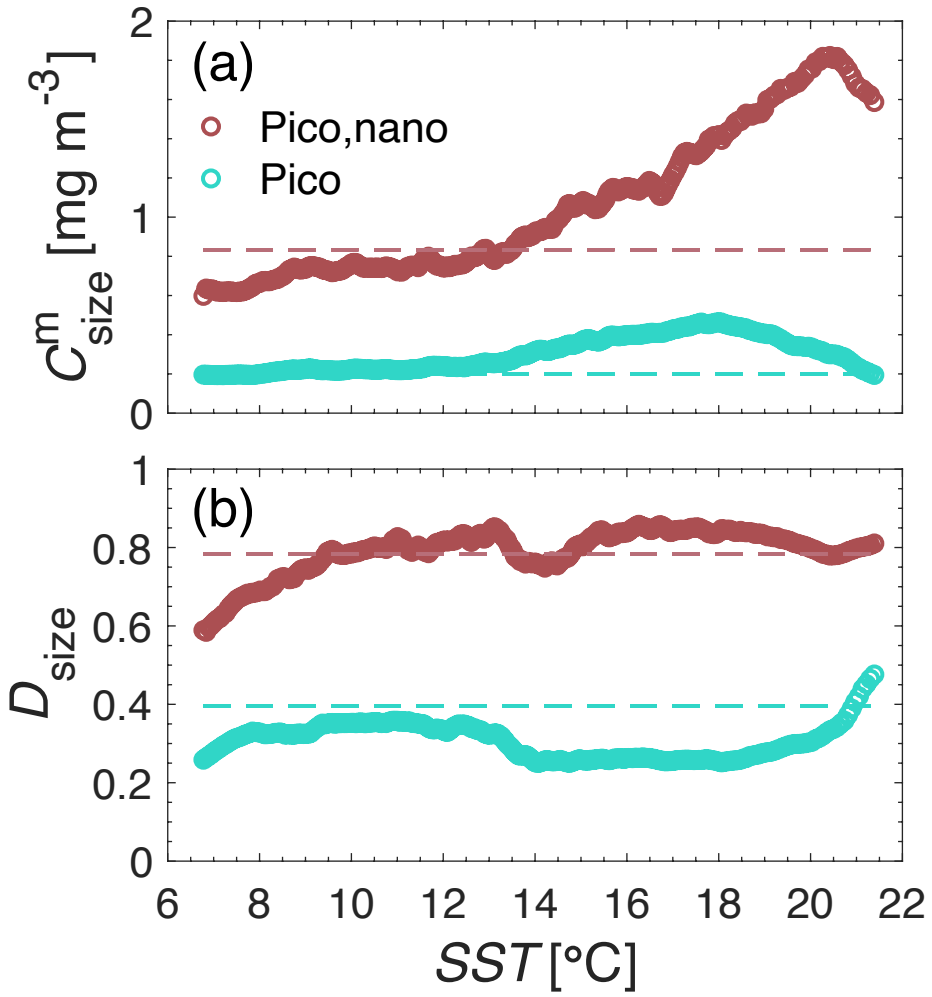

Figure 4 Brewin et al. (2010) model parameters (a) $C^m_{pico,nano}/C^m_{pico}$*, and (b)* $D_{pico,nano}/D_{pico}$ *as a function of* SST*. Circle markers show the median parameter values obtained by performing a running bootstrap fit of the model (Eqs. 9 and 10) to the* in situ *parameterization data set (*N = *418) sorted by increasing* SST*. The* SST*-parameter relationships were smoothed using a 5-point running average. Dashed lines indicate the* SST*-independent model (B-NES) parameters obtained when fitting the model to the full parameterization data set.*

the parameters of the B10 model. This was done by sorting the pigment-based estimates of F_{pico} and $F_{pico,nano}$ from the parameterization data set by increasing *SST* and conducting a running fit of the model from low to high *SST,* using a bin size of 125 samples. Starting at the lowest temperature, the bin was moved at one-sample intervals, and at each interval Eqs. (9) and (10) were fit to the data within the bin using the same the same approach as described in the previous section. From each fit, the median values of the model parameters C^m_{size} and D_{size}, along with the average *SST* of the binned data,

were incorporated into a LUT. Finally, the LUT relationships were smoothed using a 5-point running mean (Fig. 4). We chose a LUT approach as opposed to fitting logistic functions to represent the *SST*-parameter relationships in order to capture variability in the relationships that may be ecological meaningful and would otherwise be smoothed out by a logistic curve. The LUT included 293 unique sets of model parameters covering a range of *SST* of 6.8 – 21.4 ºC at intervals of approximately 0.06 ºC. Application of the LUT enables a dynamic set of model parameters to be derived based on remotely sensed *SST*. We refer to this *SST*-dependent re-parameterization as B-NES-*SST* henceforth.

2.7.2 Absorption-based

2.7.2.1 Ciotti et al. (2002)

The model of Ciotti et al. (2002) (denoted C02) estimates the fractional contribution of picoplankton (F_{pico}), by weighting $a_{ph}^*(\lambda)$ between two basis spectra representing "pure" micro- and picoplankton. The basis spectra were determined by lab measurements of $a_{ph}(\lambda)$ of 16 natural phytoplankton communities of varying dominant cell sizes, and are provided in Ciotti et al. (2002) with an updated picoplankton spectra provided by Ciotti and Bricaud (2006). The model can be expressed as:

$$a_{ph}^*(\lambda) = \left[F_{pico} \ * \ \bar{a}_{pico}^*(\lambda)\right] + \left[\left(1 - F_{pico}\right) \ * \ \bar{a}_{micro}^*(\lambda)\right], \qquad (17)$$

where $\bar{a}^*_{pico}(\lambda)$ and $\bar{a}^*_{micro}(\lambda)$ represent the basis spectra of pico- and microplankton, respectively. F_{pico} was estimated from Eq. (17) by performing a linear least squares optimization (MATLAB function *lsqlin.m*), using satellite-derived $a_{ph}^*(\lambda)$ (calculated by dividing the satellite $a_{ph}(\lambda)$ by the satellite [*Chl-a*]) and the published basis spectra at four wavelengths (443, 490, 510, and 555 nm). These four wavelengths were used due to the poor retrieval of $a_{ph}(670)$ (see Section 3.1) and better statistical performance when

excluding 412 nm. The inverse of F_{pico} ($1 - F_{pico}$) was considered equivalent to the combined fraction of micro- and nanoplankton ($F_{micro,nano}$).

2.7.2.2 Mouw and Yoder (2010)

The algorithm of Mouw and Yoder (2010) (denoted MY10) employs an optical LUT containing ranges of F_{micro} (binned to increments of 0.1), [*Chl-a*], and $a_{dg}(443)$, from which $R_{rs}(\lambda)$ was calculated using the radiative transfer software HydroLight (Mobley and Sundman, 2013). The model uses satellite [*Chl-a*] and $a_{dg}(443)$ as inputs to first narrow the search space of the LUT, then the closest matching LUT $R_{rs}(443)$ to the satellite-derived $R_{rs}(443)$ is found to retrieve the corresponding F_{micro}. $F_{pico,nano}$ is then calculated as $1 - F_{micro}$. Based on determined thresholds for the detectability of cell size from SeaWiFS $R_{rs}(\lambda)$ (Mouw and Yoder, 2010), the algorithm masks pixels with [*Chl-a*] < 0.05 mg m^{-3}, [*Chl-a*] > 1.75 mg m^{-3}, or $a_{dg}(443) > 0.17$. Additionally, when applied to a satellite image, a 2D-averaging filter (MATLAB function *filter2.m*) with a 3x3 pixel size is applied in the algorithm routine.

2.8 Model assessment and imagery application

PSC algorithm performance was assessed statistically (see Section 2.5) as follows. First, using the *in situ* [*Chl-a*] data as input, estimates of F_{size} and C_{size} from the *SST*-independent abundance-based models (B10, B15, B17, D11, H11, MB20, B-NES, and H-NES) were compared with the *in situ* pigment-based estimates of F_{size} and C_{size} for both the parameterization and validation data sets. Then, using the *in situ* [*Chl-a*] and matching satellite *SST* as input, estimates of F_{size} and C_{size} from the *SST*-dependent models (B17-*SST*, MB20-*SST*, B-NES-*SST*) were also compared with the *in situ* F_{size} and C_{size} from both the parameterization and validation data sets, and the influence of *SST* on

model performance relative to the *SST*-independent models was quantified. Lastly, using the satellite products as input, independent satellite validation of C_{size} was conducted for the regionally re-parameterized abundance-based models (B-NES-*SST*, B-NES, and H-NES) and the absorption-based algorithms (C02 and MY10).

To illustrate the application of the models to ocean color imagery and explore spatial-seasonal variations of PSCs in the NES region, the best performing abundance-based and absorption-based models were applied to monthly imagery composites for April 2019 and September 2019, and qualitatively compared.

3. Results

3.1 Satellite validation of [Chl-a], $a_{ph}(\lambda)$ and $a_{dg}(\lambda)$

As the performance of PSC algorithms is largely dependent on the quality of the satellite products used as inputs, the satellite retrievals of [*Chl-a*], $a_{ph}(\lambda)$ and $a_{dg}(\lambda)$ in the NES were first validated with the available *in situ* observations. Of the two [*Chl-a*] algorithms assessed, the standard OC-CCI algorithm (Fig. 5a) displayed lower difference and bias (*MAD* = 0.21, δ = -0.03) than the regional empirical algorithm of Pan et al. (2010) (*MAD* = 0.27, δ = -0.20; Fig. 5b) when compared with the *in situ* HPLC [*Chl-a*]. The OC-CCI algorithm was associated with overestimation at low [*Chl-a*] and underestimation at high [*Chl-a*] (>0.6 mg m^{-3}). This is a relatively common feature of [*Chl-a*] estimated from empirical band-ratio algorithms (e.g., OCx), that can be attributed primarily to the impact of phytoplankton cell size and underlying variability in the concentrations of CDOM and inorganic particulates (Dierssen, 2010; Mouw et al., 2012; Sauer et al., 2012). In contrast, the algorithm of Pan et al. (2010) exhibited a systematic underestimation across the entire

[*Chl-a*] range (δ = -0.20). This difference is reflected in a lower Type-II regression slope for the OC-CCI algorithm (*S* = 0.66) compared with a slope closer to one for the Pan et al. (2010) algorithm (*S* = 0.89). The two algorithms displayed similar correlation coefficients (*r* = 0.75 and 0.74 respectively). The performance of the OC-CCI algorithm was comparable to the global [*Chl-a*] validation of OC-CCI v4.2 as shown in the Product User Guide (*RMSD* = 0.32, δ = 0.07, *r* = 0.75, *S* = 0.72; see their Fig. 5). Considering the lower difference and bias of the OC-CCI product, [*Chl-a*] from this algorithm was used as the satellite input to the PSC models in this study.

The standard OC-CCI estimates of $a_{ph}(\lambda)$ and $a_{dg}(\lambda)$, derived using QAA_v5, compared reasonably with *in situ* measurements, with most points falling within the $\pm$ 30% uncertainty range at the wavelengths 443, 490, and 510 nm (Fig. 5 c-h). The lowest differences for $a_{ph}(\lambda)$ were observed at 490 and 510 nm (*MAD* = 0.22 and 0.24, respectively), with retrievals of $a_{ph}(443)$ exhibiting slightly higher uncertainty (*MAD* = 0.28). For $a_{dg}(\lambda)$, the best performance was observed at 443 nm (*MAD* = 0.17, δ = -0.14). There was a consistent negative bias in the retrieved $a_{dg}(\lambda)$ which became more negative at longer wavelengths, corresponding with an increasingly positive bias for $a_{ph}(\lambda)$. Retrievals of $a_{ph}(555)$ and $a_{ph}(670)$ were associated with larger errors (*MAE* = 0.32 and 0.62, respectively), the same being true for $a_{dg}(555)$ and $a_{dg}(670)$ (*MAE* = 0.38 and 0.41, respectively). The decrease in performance at longer wavelengths for QAA_v5 is consistent with results from the global inter-comparison of bio-optical algorithms conducted by Brewin et al. (2015b) (Model E in their study). Considering the reasonable performance of the standard OC-CCI $a_{ph}(\lambda)$ and $a_{dg}(443)$ products (443 nm is the only

wavelength required for $a_{dg}(\lambda)$ as input into the MY10 algorithm), no regional optimization of the absorption retrievals was attempted in this study.

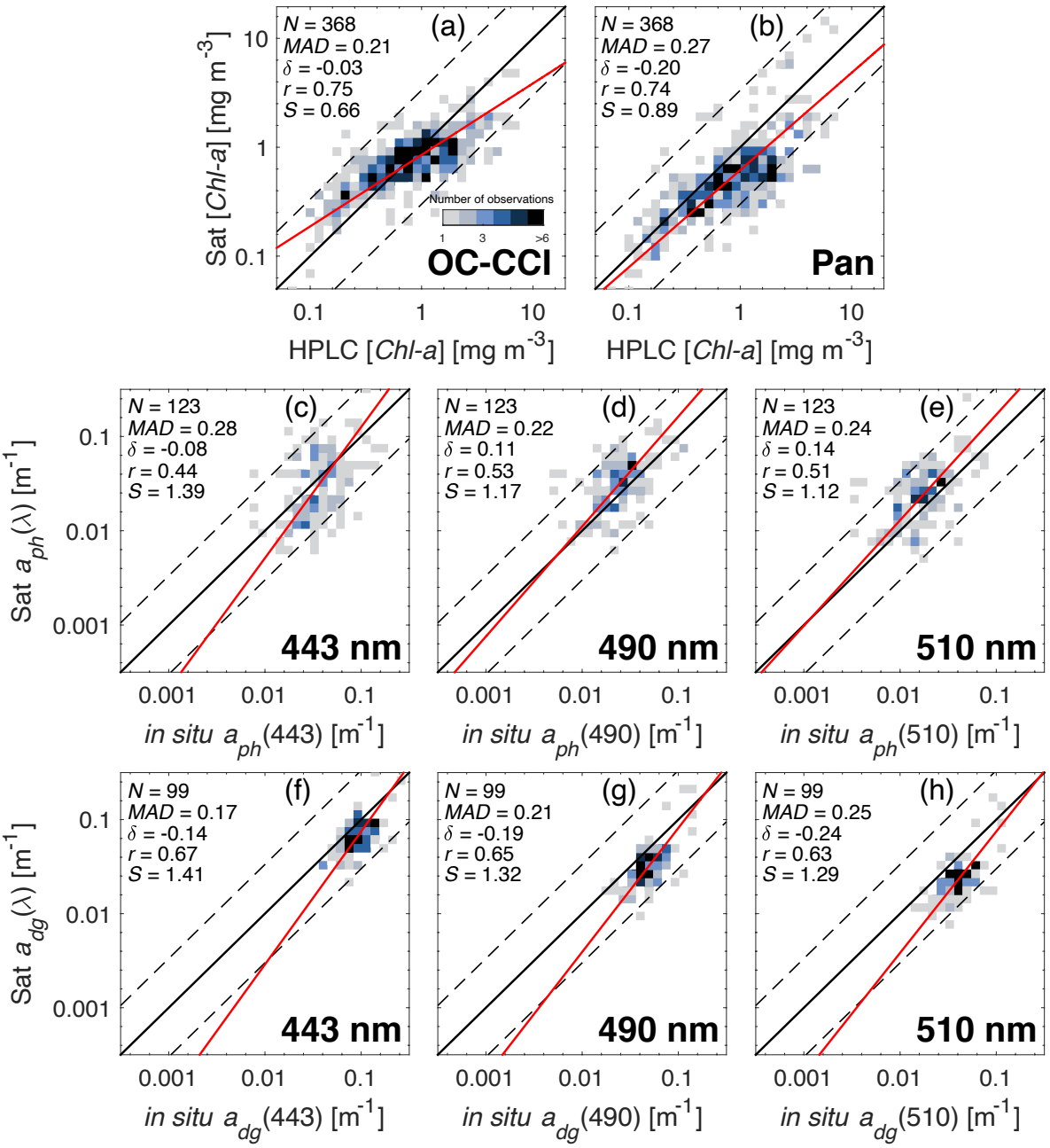

*Figure 5 Bivariate histograms showing the satellite-to-*in situ *comparisons of* [Chl-a]*,* $a_{ph}(\lambda)$*, and* $a_{dg}(\lambda)$*, shaded by number of observations: (a)* [Chl-a] *from the standard OC-CCI algorithm, (b)* [Chl-a] *from the regional algorithm of Pan et al. (2010), (c)* $a_{ph}(443)$*, (d)* $a_{ph}(490)$*, (e)* $a_{ph}(510)$*, (f)* $a_{dg}(443)$*, (g)* $a_{dg}(490)$*, and (h)* $a_{dg}(510)$ *from the standard OC-CCI algorithm (QAA_v5). The solid black line is the 1:1 line, dashed black lines indicate the 1:1 line* $\pm$ *30%, and the red line is the Type-II regression line.* N *denotes the number of match-ups,* MAD *denotes the mean absolute difference,* δ *denotes the bias,* r *denotes the correlation coefficient, and* S *denotes the regression slope. The* $a_{ph}(\lambda)$ *and* $a_{dg}(\lambda)$ *data are shown using the same x- and y-axis range for comparison.*

3.2 Comparison of SST-independent abundance-based models

Figure 6 shows the *in situ* pigment-based estimates of F_{size} and C_{size} from the parameterization data set (N = 418) with the *SST*-independent abundance-based models overlain. F_{size} and C_{size} exhibited trends with C_{HPLC} that are consistent with established relationships of phytoplankton size structure and total biomass (Brewin et al., 2010; Hirata et al., 2011; Uitz et al., 2006). F_{micro} generally increased, while $F_{pico,nano}$, and F_{pico} generally decreased with increasing C_{HPLC}. F_{nano} displayed a unimodal relationship C_{HPLC}, peaking at intermediate C_{HPLC}. C_{micro} increased in near log-linear fashion with C_{HPLC}, becoming more tightly correlated at higher $C_{HPLC,}$ when microplankton are the dominant size class. $C_{pico,nano}$, C_{nano}, and C_{pico}, also displayed an overall positive relationship with C_{HPLC}, with greater variability at higher C_{HPLC}. The abundance-based models all followed to first order these general trends, with some variations that can be attributed to differences in the model frameworks, data sets, and approaches used for model development/parameterization. For example, the B10 model parameters $C^m_{pico,nano}$ and C^m_{pico} impose asymptotic maximum values for $C_{pico,nano}$ and C_{pico} respectively, while the purely empirical H11 model does not define any strict maximums. This can be seen when comparing C_{pico} predicted by the H-NES model, which increases continuously with C_{HPLC}, with that of the B-NES model, which levels off at the imposed maximum concentration (C^m_{pico} = 0.2 mg m^{-3}) (Fig. 6h). The H11-modeled F_{pico} is based on a different empirical function (Eq. 15) than the one used in this study (see Section 2.7.1.6), and goes to zero at C_{HPLC} > 4 mg m^{-3} (Fig. 6d), accounting for the breakdown in this model at higher C_{HPLC} for C_{pico}, C_{nano}, and $C_{pico,nano}$ (Fig. 6f-h). Compared with the other models, the B-NES

model predicted a slightly higher F_{micro} and lower $F_{pico,nano}$ and F_{pico} at low C_{HPLC} (Fig. 6a,b,d).

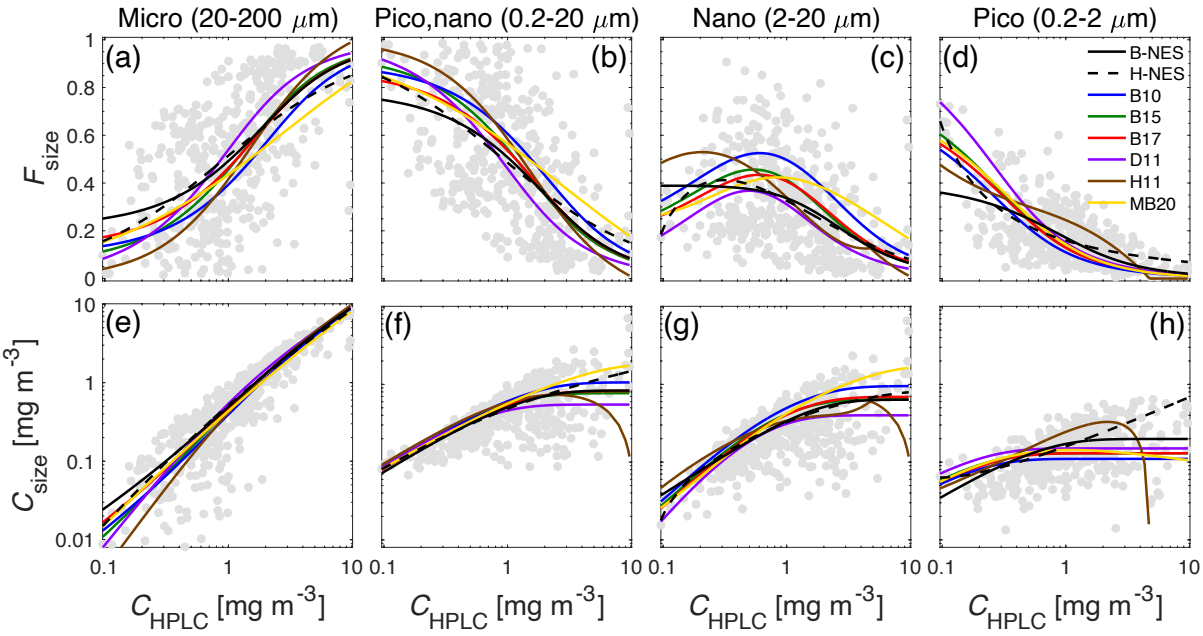

Figure 6 Pigment-based estimates of F_{size} (a-d) and C_{size} (e-h) as a function of C_{HPLC} from the parameterization data set (N = 418) with abundance-based models overlaid: re-parameterized B10 model (B-NES, solid black), re-parameterized H11 model (H-NES, dashed black), Brewin et al., 2010 (B10, blue), Brewin et al., 2015a (B15, green), Brewin et al., 2017 (B17, red), Devred et al., 2011 (D11, violet), Hirata et al., 2011 (H11, brown), and Moore and Brown, 2020 (MB20, yellow).

Furthermore, the B-NES-modeled F_{nano} leveled off at low C_{HPLC} rather than decreasing as with the other models (Fig. 6c). Despite the variability between the different models, the range of variability in the pigment-based estimates of F_{size} and C_{size} was generally greater across the entire trophic domain. Statistical comparison between the *in situ* and modeled F_{size} and C_{size} for both the parameterization and validation data sets yielded very similar metrics between models (Appendix A). Overall, minimal improvement in performance was observed for the regionally re-parameterized models (B-NES and H-NES) compared with the other models examined, although there was a reduction in error and bias for the nanoplankton size class compared with the original global models (B10 and H11).

3.3 Regional SST-dependent model (B-NES-SST)

Figure 7 shows the modeled F_{size} and C_{size} from the B-NES-*SST* model as a function of [*Chl-a*] at varying *SST* along with the *SST*-independent (B-NES) model for reference. *SST* had a clear influence on the predicted F_{size} and C_{size} for all of the size classes. Lower *SST* was associated with a higher fraction of microplankton, and a lower fraction of nanoplankton and picoplankton (Fig. 7a-d), consistent with the results of previous studies (Brewin et al., 2017b; Moore and Brown, 2020; Sun et al., 2019b). This relationship was generally observed across the entire [*Chl-a*] domain but was more pronounced at lower [*Chl-a*]. F_{nano} increased with *SST* for [*Chl-a*] > 1 mg m^{-3}, whereas for [*Chl-a*] < 1 mg m^{-3}, F_{nano} increased with *SST* only up to ~18 ºC, beyond which there was a decrease in F_{nano} corresponding with an increase in F_{pico} at *SST* > 18 ºC. The largest variability in modeled C_{micro} with *SST* was at [*Chl-a*] < 1 mg m^{-3}, whereas the largest variability in modeled $C_{pico,nano}$, C_{nano}, and C_{pico} with *SST* was at [*Chl-a*] > 1 mg m^{-3} (Fig. 7e-h).

Results from the statistical comparison of modeled F_{size} and C_{size} from the B-NES-*SST*, B17-*SST*, and MB20-*SST* models with the *in situ* pigment-based estimates of F_{size} and C_{size} are presented in Table 5. For both the parameterization and validation data sets, the B-NES-*SST* model performed with lower error and significantly higher correlation coefficients than the other two *SST*-dependent models across all size classes. There was also a consistent improvement in performance (i.e., reduction in error, increase in correlation coefficient) for the B-NES-*SST* model relative to the *SST*-independent B-NES model for both data sets. Considering the statistical results from the validation set, the inclusion of *SST* led to a reduction in *MAD* of 10-12% for F_{size} and 4-10% for C_{size}, with

the largest reductions for F_{nano} and $C_{pico,nano}$, respectively. Likewise, the inclusion of *SST* increased the correlation coefficient (r) for F_{size} and C_{size}, with the largest increases for F_{nano} and C_{pico}, respectively. Interestingly, the B17-*SST* model exhibited slightly worse performance relative to the *SST*-independent B17 model for estimating F_{micro}, $F_{pico,nano}$, and $C_{pico,nano}$, with essentially no change for C_{micro}. The MB20-*SST* model displayed general improvement over the MB20 model.

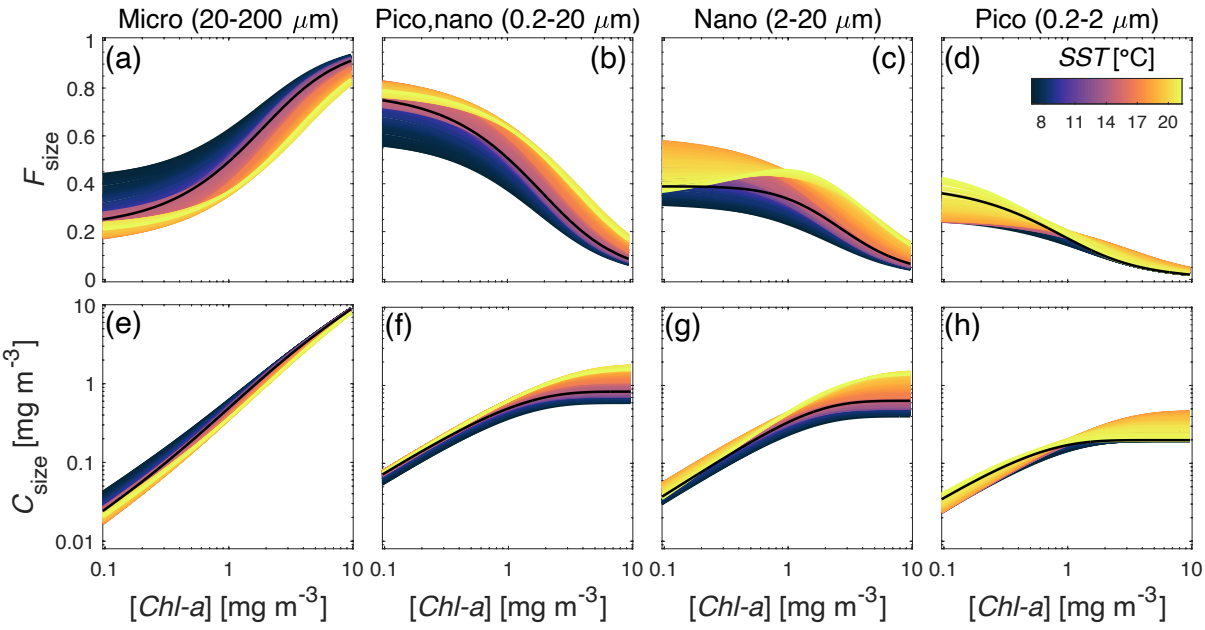

Figure 7 Modeled F_{size} *(a-d) and* C_{size} *(e-h) from the B-NES-SST model plotted as a function of [Chl-a], with the color gradient illustrating the changes in the model when model parameters vary as a function of SST (see Section 2.7.1.7, Fig. 4). The black line indicates the SST-independent model, with a single set of model parameters (B-NES).*

Table 5. Mean absolute difference (*MAD*) and correlation coefficients (*r*) for F_{size} and C_{size} (values for C_{size} shown in parentheses) for the *SST*-dependent abundance-based models applied to the *in situ* parameterization and validation data sets. The percent change in the metrics when incorporating *SST* relative to the *SST*-independent models is included for reference. Percentages are rounded to the nearest 1%.

Parameter	*Model*	*in situ parameterization set (N = 418)*				*in situ validation set (N = 368)*			
		MAD	*% change with SST*	*r*	*% change with SST*	*MAD*	*% change with SST*	*r*	*% change with SST*
F_{micro} (C_{micro})	B-NES-*SST*	0.16 (0.21)	-11 (-13)	0.68 (0.89)	+21 (+3)	0.17 (0.24)	-11 (-4)	0.58 (0.87)	+32 (+2)
	B17-*SST*	0.19 (0.23)	+6 (-4)	0.54 (0.87)	-4 (+1)	0.20 (0.25)	+5 (0)	0.44 (0.85)	0 (0)
	MB20-*SST*	0.18 (0.23)	-5 (-4)	0.59 (0.83)	+7 (-3)	0.19 (0.24)	-5 (-4)	0.49 (0.86)	+9 (+1)
$F_{pico,nano}$ ($C_{pico,nano}$)	B-NES-*SST*	0.16 (0.17)	-11 (-11)	0.68 (0.75)	+21 (+12)	0.17 (0.18)	-11 (-10)	0.58 (0.77)	+32 (+6)
	B17-*SST*	0.19 (0.20)	+5 (+5)	0.54 (0.59)	-4 (-11)	0.20 (0.20)	+5 (0)	0.44 (0.72)	0 (+1)
	MB20-*SST*	0.18 (0.20)	-5 (0)	0.59 (0.56)	+7 (-16)	0.19 (0.19)	-5 (-5)	0.49 (0.73)	+9 (0)
F_{nano} (C_{nano})	B-NES-*SST*	0.13 (0.21)	-13 (-13)	0.55 (0.74)	+49 (+12)	0.15 (0.26)	-12 (-7)	0.39 (0.79)	+225 (+6)
	B17-*SST*	0.14 (0.24)	-7 (-4)	0.44 (0.66)	+19 (0)	0.16 (0.27)	-6 (-4)	0.29 (0.75)	+45 (+1)
	MB20-*SST*	0.16 (0.26)	-6 (-4)	0.28 (0.58)	+8 (-13)	0.16 (0.27)	-11 (-7)	0.18 (0.72)	0 (-3)
F_{pico} (C_{pico})	B-NES-*SST*	0.07 (0.19)	-13 (-10)	0.70 (0.64)	+15 (+16)	0.09 (0.20)	-10 (-9)	0.73 (0.62)	+16 (+15)
	B17-*SST*	0.08 (0.23)	0 (-4)	0.63 (0.46)	0 (+7)	0.09 (0.23)	-10 (-4)	0.73 (0.53)	+4 (+23)
	MB20-*SST*	0.08 (0.21)	0 (-13)	0.67 (0.53)	+6 (+56)	0.10 (0.22)	0 (-8)	0.72 (0.52)	+3 (+37)

3.4 Satellite validation of C_{size}

Using the satellite-derived data as input, estimates of C_{size} from the regional abundance-based (B-NES-*SST*, B-NES, and H-NES) and absorption-based algorithms (C02 and MY10) were compared with the *in situ* pigment-based C_{size} from the independent validation data set. The B-NES-*SST*, B-NES, and H-NES models displayed similar statistical performance (Fig. 8), although the *SST*-dependent model performed considerably better across all statistical metrics for C_{micro} (Fig. 8a). The B-NES-*SST* model

generally performed better than the *SST*-independent B-NES model, and was less constrained by static maximums for $C_{pico,nano}$, C_{nano}, and C_{pico} (Fig. 8 f-h, dashed green lines), particularly for C_{pico}, for which a substantial increase in the correlation coefficient was observed, consistent with previous studies (Brewin et al., 2017b; Sun et al., 2019b). Like the OC-CCI [*Chl-a*] input product, the satellite-estimated C_{size} from these models tended to be underestimated at higher concentrations and overestimated at low concentrations, especially for C_{nano} and C_{pico} <0.1 mg m^{-3} and 0.05 mg m^{-3}, respectively.

The C02 and MY10 algorithms performed comparably to the re-parameterized abundance-based models (Fig. 9). The MY10 algorithm estimated C_{micro} and $C_{pico,nano}$ with similar differences as the B-NES-*SST* model, but with higher correlation coefficients (r = 0.74 and 0.63, respectively) and improved regression slopes (S = 0.97 and 0.89, respectively), although it is noted that the number of validation points was reduced from N = 368 to N = 352 and N = 332 for C02 and MY10, respectively. For the former, this was due to 16 match-ups with negative satellite $a_{ph}(555)$ retrievals, while for the latter, 36 match-ups exceeded the [*Chl-a*] and $a_{dg}(443)$ detection thresholds of the MY10 algorithm (1.75 mg m^{-3} and 0.17 m^{-1}, respectively; see Sections 2.7.2.1 and 2.7.2.2). Although the overall bias was generally higher for the absorption-based approaches, they did not exhibit the same overestimation (underestimation) at low (high) concentrations as seen with the abundance-based methods, with the exception of $C_{micro,nano}$ estimated by C02 model (Fig. 9a).

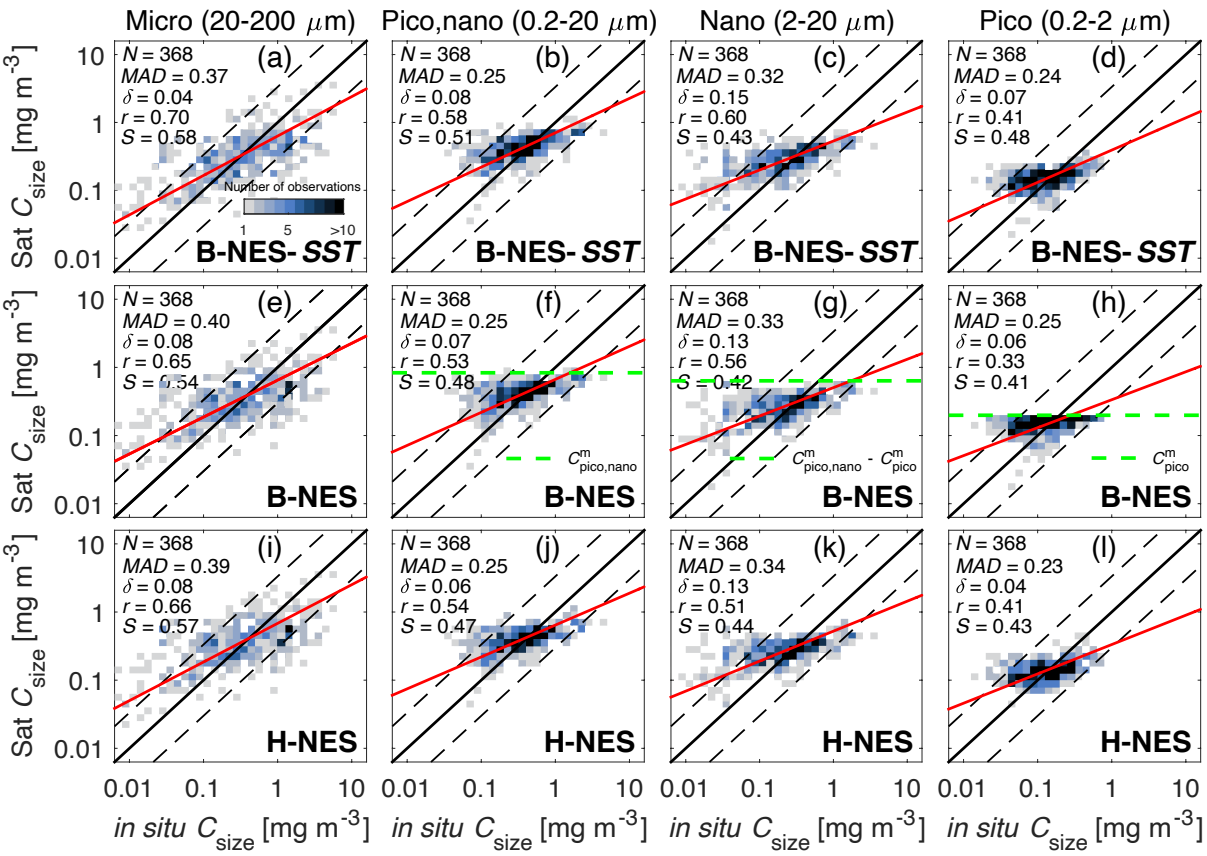

*Figure 8 Bivariate histograms showing the satellite-to-*in situ *comparisons of* C_{size} *estimated from the regionally parameterized B-NES-*SST *(a-d), B-NES (a-d), and H-NES (i-l) abundance-based models, shaded by number of observations. The solid black line is the 1:1 line, dashed black lines indicate the 1:1 line ± 30%, and the red line is the Type-II regression line. Dashed green lines indicate the maximum chlorophyll concentrations imposed by the B-NES model.* N *denotes the number of match-ups for each parameter,* MAD *denotes the mean absolute difference,* δ *denotes the bias,* r *denotes the correlation coefficient, and* S *denotes the regression slope.*

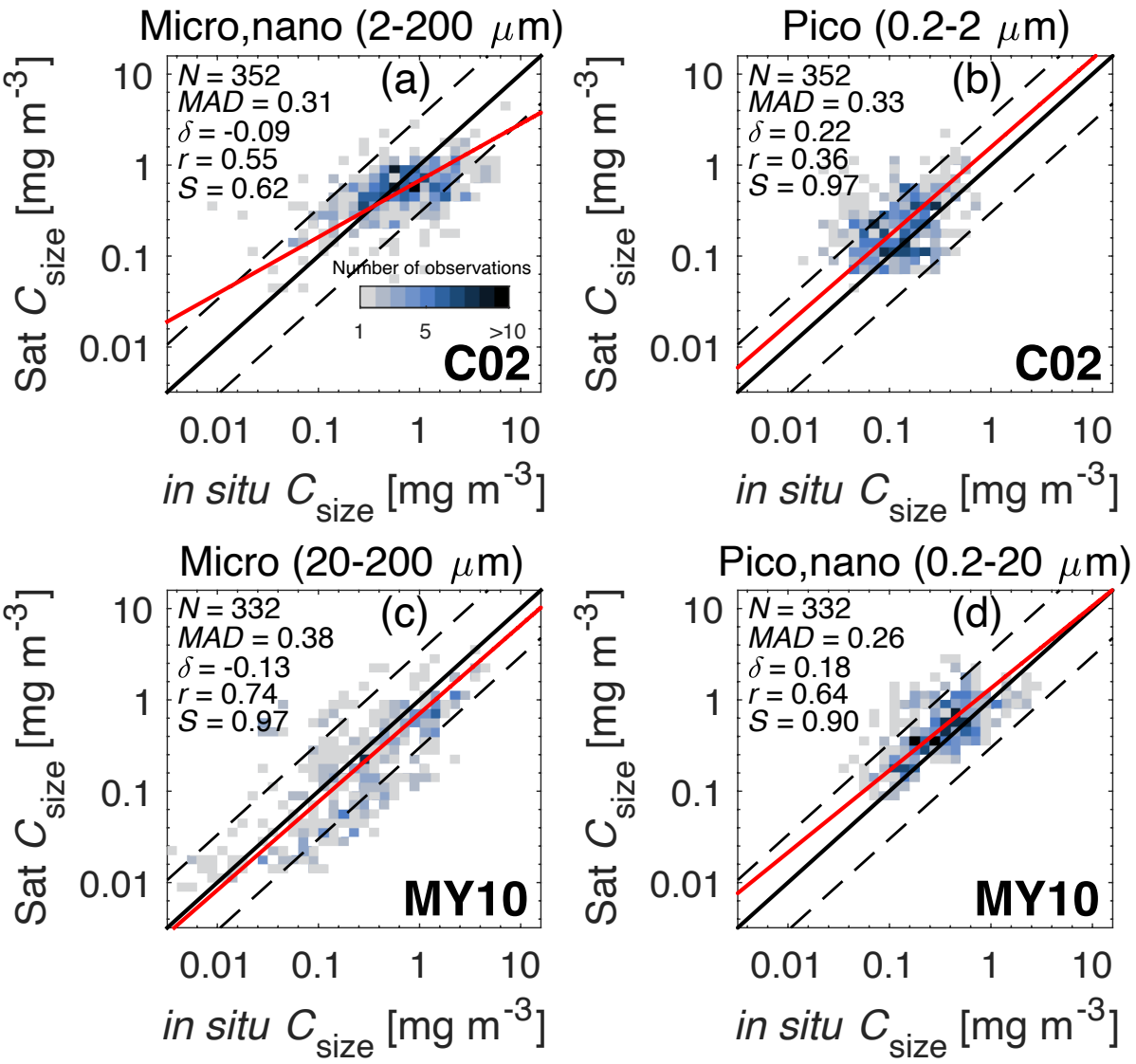

*Figure 9 Bivariate histograms showing the satellite-to-*in situ *comparisons of* C_{size} *estimated from the absorption-based algorithms applied in this study: (a)* $C_{micro,nano}$ *and (b)* C_{pico} *from the algorithm of Ciotti et al. (2002) and (c)* C_{micro} *and (d)* $C_{pico,nano}$ *from the algorithm of Mouw and Yoder (2010). The solid black line is the 1:1 line, dashed black lines indicate the 1:1 line ± 30%, and the red line is the Type-II regression line.* N *denotes the number of match-ups,* MAD *denotes the mean absolute difference,* δ *denotes the bias,* r *denotes the correlation coefficient, and* S *denotes the regression slope.*

3.5 Examples of satellite imagery

Considering the overall improved performance of the B-NES-*SST* algorithm compared with the other abundance-based models, and the statistically similar comparison metrics of the MY10 absorption-based approach, monthly composite imagery from these algorithms was generated for April 2019 and September 2019 for visualization

and spatial-temporal comparison. These months were chosen as they were relatively cloud free and displayed contrasting *SST* and [*Chl-a*], thus providing some insight into the seasonal variability of phytoplankton size structure in the NES.

Figure 10 shows the monthly imagery of OC-CCI [*Chl-a*] (Fig. 10a) and MUR *SST* (Fig. 10b), along with the size class fractions (F_{micro}, F_{nano}, F_{pico}; Fig.10c-e) and size-specific [*Chl-a*] (C_{micro}, C_{nano}, C_{pico}; Fig.10f-h) from the B-NES-*SST* algorithm for April 2019. In April, around the time of the typical North Atlantic spring bloom (Friedland et al., 2016), [*Chl-a*] exceeding 1 mg m^{-3} was observed both on the shelf and off-shore, with the highest [*Chl-a*] observed around GB, south of Nova Scotia, and in the near-shore coastal waters along the MAB and GoM. *SST* ranged from <5 ºC in the northern GoM to ~25 ºC within the Gulf Stream. Microplankton were dominant in low *SST*, high [*Chl-a*] waters in the GoM, on GB, along the coast, and within the major estuaries. Nanoplankton were most prevalent in the intermediate [*Chl-a*] and *SST* waters off-shore. Picoplankton was the dominant size class in the oligotrophic, high *SST* surface waters of the Gulf of Stream.

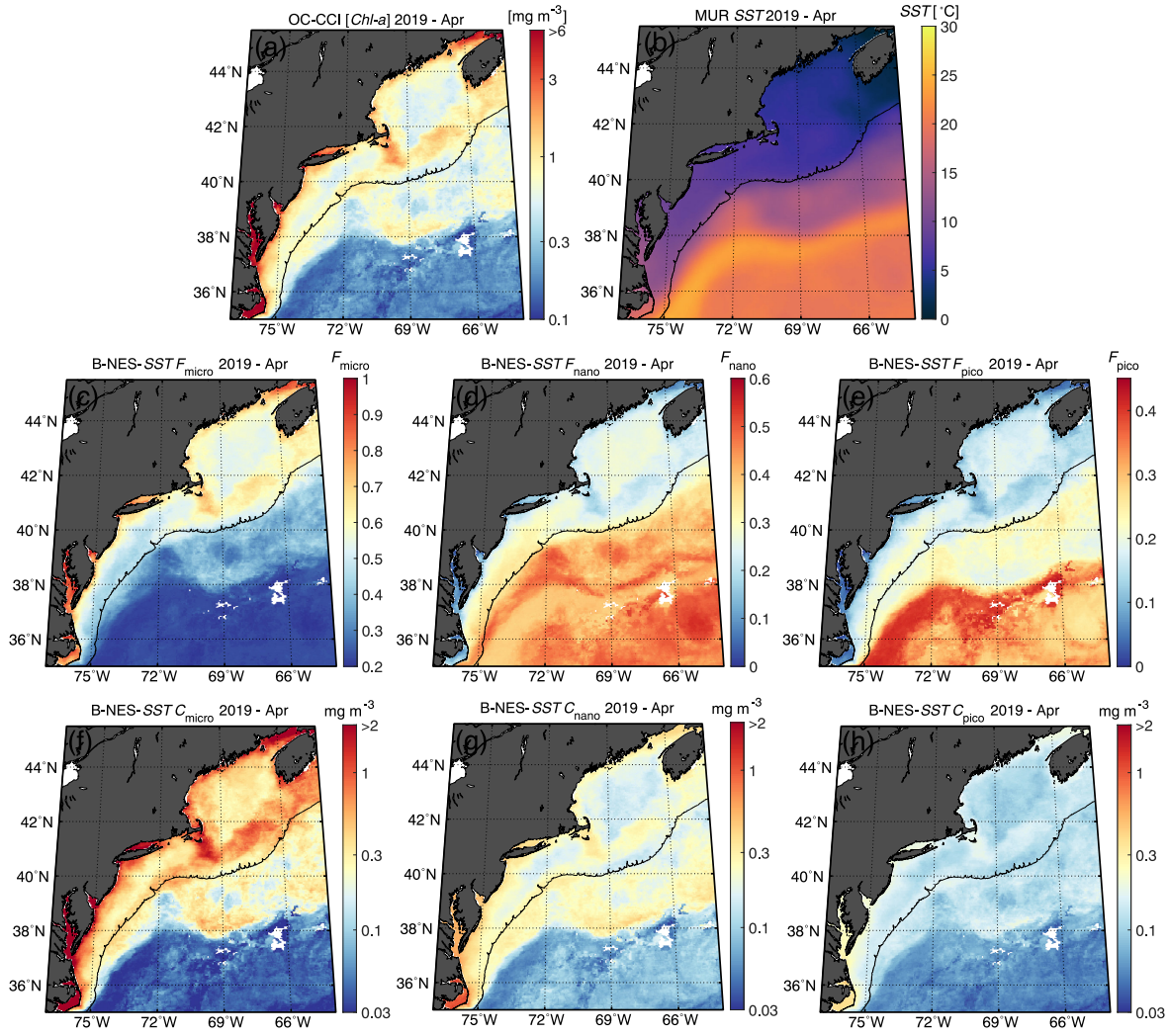

*Figure 10 Monthly composite imagery for April 2019: (a) OC-CCI [*Chl-a*], (b) MUR* SST*, (c)* F_{micro}*, (d)* F_{nano}*, (e)* F_{pico}*, (f)* C_{micro}*, (g)* C_{nano}*, and (h)* C_{pico} *from the B-NES-*SST *model. Color scales for* F_{size} *are adjusted to reflect the range of the model for each size class (see Fig. 8). The black line indicates the 400 m isobath to mark the approximate location of the shelf break.*

Figure 11 shows the same as Figure 10 but for September 2019. Compared with April, in September areas of [*Chl-a*] > 1 mg m^{-3} did not extend as far off-shore but were mainly confined to near-shore regions of the MAB, the GoM, and GB. There was a strong gradient in [*Chl-a*] from the highly productive waters along the coast and to the north to the oligotrophic ([*Chl-a*] < 0.1 mg m^{-3}) off-shore waters to the south. *SST*

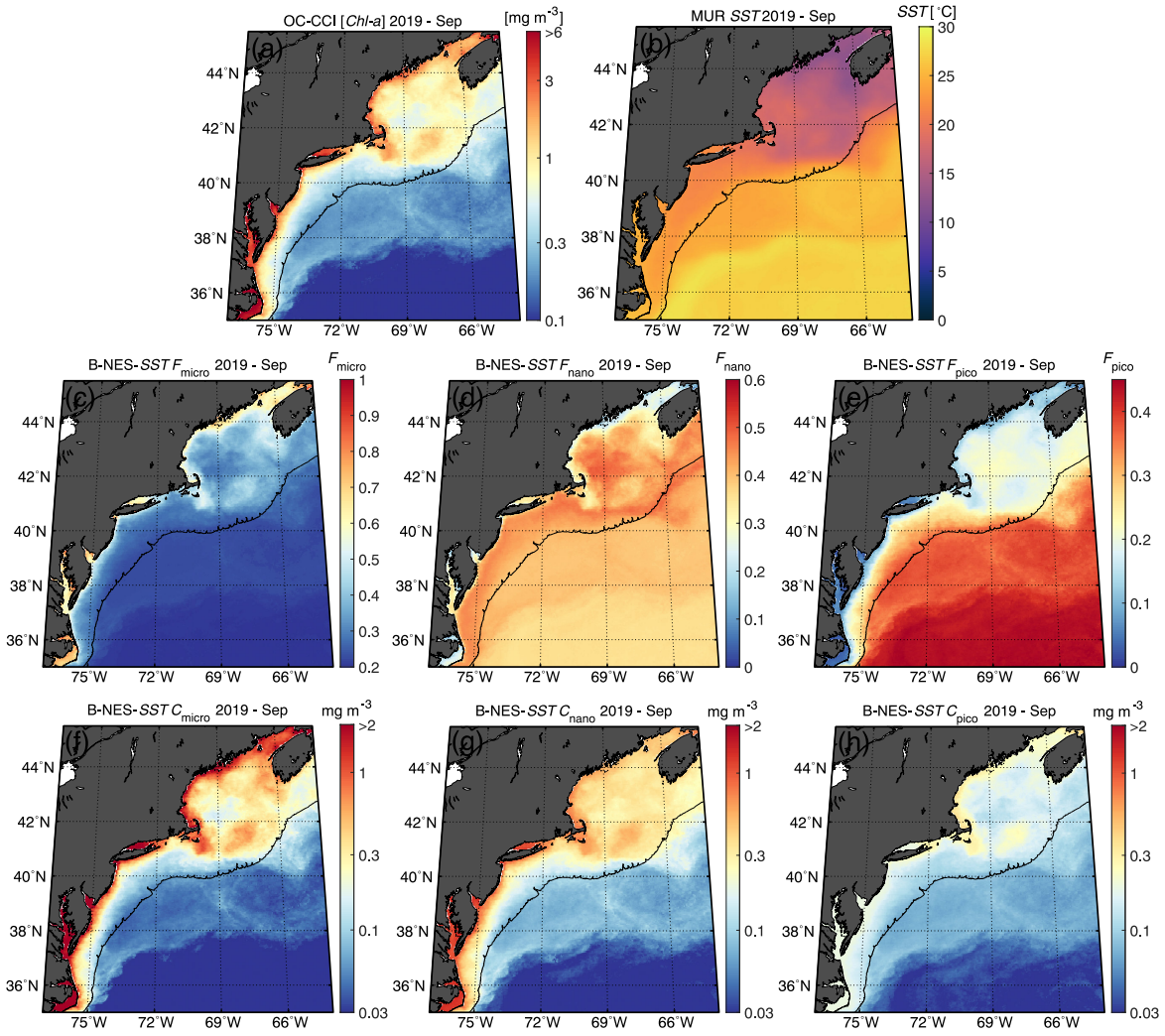

*Figure 11 Monthly composite imagery for September 2019: (a) OC-CCI [*Chl-a*], (b) MUR* SST*, (c)* F_{micro}*, (d)* F_{nano}*, (e)* F_{pico}*, (f)* C_{micro}*, (g)* C_{nano}*, and (h)* C_{pico} *from the B-NES-*SST *model, as per the previous figure.*

exceeded 20 ºC throughout much of the region, with cooler *SST* observed to the north around GB and within the GoM, coinciding with the higher [*Chl-a*] observed in these areas. Microplankton comprised a smaller fraction of [*Chl-a*] in both near-shore and off-shore waters in September, with nanoplankton becoming more dominant on the shelf, particularly in the central GoM and areas immediately surrounding GB. Likewise, the contribution of nanoplankton generally decreased off-shore in September, with

picoplankton becoming more dominant in these waters, coinciding with higher *SST* and lower [*Chl-a*] than was observed in April.

A comparison of F_{micro} imagery from the B-NES-*SST* and MY10 algorithms for April 2019 and September 2019 is presented in Figure 12. Considering the F_{micro} output from the MY10 algorithm is binned to increments of 0.1, the color scale for the B-NES-*SST* imagery was adjusted to match the scale of the MY10 imagery to facilitate a more visually equitable comparison. The two approaches displayed similarities and differences in the spatial patterns and extent of estimated F_{micro}. For example, both models indicated higher F_{micro} on GB and in the northern GoM than the surrounding region in September, while in April both models show areas of elevated F_{micro} extending farther offshore, beyond the shelf break. Pixels exceeding the MY10 thresholds of detection ([*Chl-a*] > 1.75 mg m^{-3} and $a_{dg}(443) > 0.17$, plotted in white) were located predominantly in shallow regions very close to shore and within major embayments, with some masked pixels on GB. While the two algorithms showed some similar spatial patterns, there were differences in the magnitude of the estimated F_{micro}. For instance, the MY10-estimated F_{micro} was higher around GB and areas in the GoM and the northern MAB than the B-NES-SST model in September, and higher within the off-shore feature of elevated [*Chl-a*] located around 38ºN, 69ºW in April. The MY10 imagery also generally showed a higher degree of spatial variability in F_{micro} compared with that of the B-NES-*SST* model. This is evident within the central GoM in April, where the MY10 imagery showed areas of F_{micro} spanning the full fractional range (i.e., 0-1), whereas the B-NES-*SST* imagery showed a much more uniform distribution of F_{micro}, ranging only between 0.5 and 0.7.

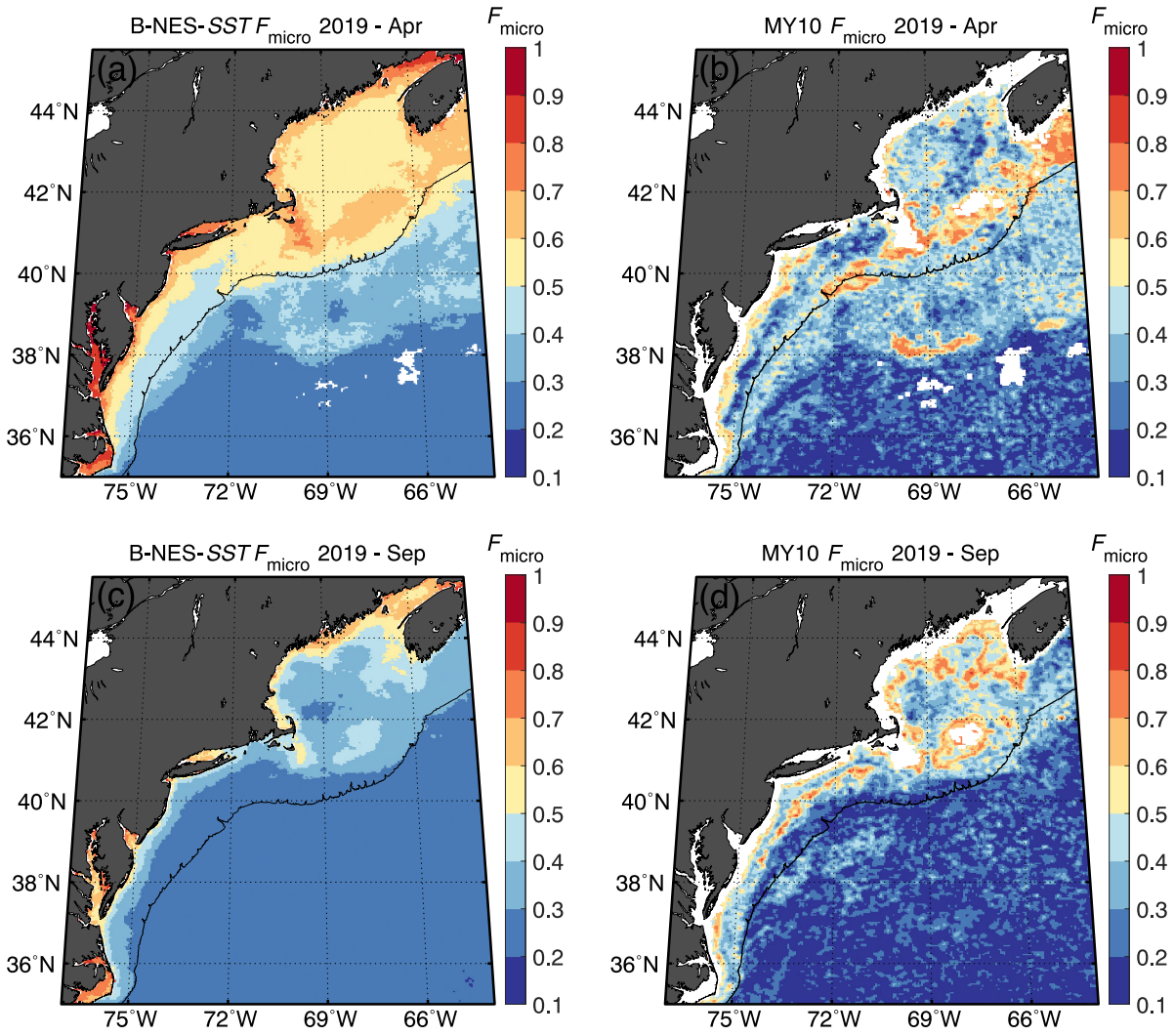

Figure 12 Comparison of monthly F_{micro} *imagery from the B-NES-*SST *and MY10 algorithms for April 2019 (a, b) and September 2019 (c, d). The MY10 algorithm applies a 2-D average filter, masks pixels that exceed defined thresholds of [*Chl-a*] and* $a_{dg}(443)$ *(plotted in white), and bins* F_{micro} *to increments of 0.1 (see Section 2.7.2.2). The color scale for the B-NES-*SST *imagery was modified to match the output of the MY10 algorithm. The black line indicates the 400 m isobath to mark the approximate location of the shelf break.*

4. Discussion and conclusions

The focus of this study was the regional refinement and evaluation of PSC algorithms in the NES. Like many similar studies, *in situ* estimates of PSCs derived from HPLC pigment data using the DPA method were used for model re-parameterization and statistical comparisons. While this approach is a popular choice given the relative abundance of HPLC samples compared with other methods for quantifying PSCs *in*

situ, it has important limitations. First, DPA is not a direct measure of cell size, but rather an approximation of size structure based on assumptions about the taxonomic groups attributed to different pigments, and the size classes represented by those taxa. In reality, pigments are not perfectly diagnostic, and are known to be shared across multiple taxa in varying concentrations dependent on physiological state (Uitz et al., 2008). Further, taxonomic groups may span multiple size classes in ways that are not fully represented by the DPA equations (Leblanc et al., 2018; Nunes et al., 2019). Although proposed modifications to account for some of these biases were incorporated in this study (Devred et al., 2011), the efficacy of this specific approach for characterizing PSCs in the NES region is uncertain and warrants further investigation. Recently, Chase et al., (2020) evaluated the DPA method by comparing pigment-based PSC estimates to coincident measurements of cell size by imaging-in-flow and conventional flow cytometry in the North Atlantic and found that DPA overestimated micro- and picoplankton and underestimated nanoplankton relative to cytometry. They recommended a revised set of DPA equations to better account for the presence of dinoflagellates and diatoms in the nanoplankton, and the presence of [*TChl-b*] in both pico- and nanoplankton. To reduce uncertainty on this front, continued efforts to inter-compare multiple *in situ* PSC methods across different oceanic environments will be extremely valuable.

Abundance-based PSC algorithms are attractive for their ease of implementation, using satellite [*Chl-a*] as the sole input parameter, and have been shown to perform well globally (Brewin et al., 2011; R. J. W. Brewin et al., 2015) and in a variety of oceanic regions (Brito et al., 2015; Di Cicco et al., 2017; Gittings et al., 2019; Sun et al., 2018).

Here, previously published abundance-based methods were tested in the NES using both original model parameters and new parameters derived from a region-specific HPLC pigment data set. Our results indicated that regional re-parameterization alone offered minimal statistical improvement compared with other models evaluated, which included both globally and regionally parameterized models. All eight of the abundance-based models tested yielded similar comparison metrics, particularly for the micro- and combined pico- and nanoplankton classes, when applied to the *in situ* [*Chl-a*] and compared with the DPA-based size class estimates from the independent *in situ* validation data set. There was more variation in the comparison metrics for separated nano- and picoplankton classes, but in no instance were the re-parameterized models exclusively the best performing, with the exception of the H-NES model for estimating picoplankton, which showed slight improvement relative to the other models when applied to both the *in situ* and satellite [*Chl-a*]. Based on the regional validation conducted in this study, the OC-CCI [*Chl-a*] product was chosen as the satellite input for model application and comparison. However, the systematic positive and negative bias of this product at low and high [*Chl-a*] respectively was directly translated to the C_{size} estimates from the regionalized abundance-based methods, underscoring the importance of the satellite [*Chl-a*] input on the accuracy and uncertainty abundance-based PSC output.

While re-parameterization alone provided little benefit in terms of improving abundance-based model performance in the NES, the incorporation of remotely sensed *SST* into the re-parameterization of the B10 model did consistently improve PSC prediction accuracy. When applied to the *in situ* validation data set, the regional *SST*-dependent B-NES-*SST* model showed a reduction in *MAD* of 10-12% for all size fractions

with respect to the *SST*-independent B-NES model. The B-NES-*SST* model also outperformed the other two *SST*-dependent models tested (B17-*SST* and MB20-*SST*) for all size classes. This result supports what has been shown by previous studies (Brewin et al., 2017b; Moore and Brown, 2020; Sun et al., 2019b; Ward, 2015) - that the addition of *SST* into abundance-based model frameworks can improve PSC prediction accuracy. The relationships between [*Chl-a*], *SST*, and phytoplankton size structure observed in this study were also in general agreement with the findings of previous studies, with lower *SST* associated with an increase in the fraction of microplankton and a decrease in the fraction of smaller cells (i.e. pico- and nanoplankton) at similar [*Chl-a*]. This relationship is not entirely surprising, given long-established connections between temperature, water-column stability, nutrient availability, and phytoplankton community size structure in the marine environment (Bouman et al., 2003; Margalef, 1978). While *SST* is used as the additional predictor variable in these models, the associated changes in size structure are not necessarily in direct response to changes in *SST* but rather the result of a combination of co-varying environmental conditions, including light availability, stratification, and nutrient availability. Further in-depth analysis of the interactions between environmental, hydrodynamic, and biogeochemical/optical parameters, similar to that conducted by Mouw et al. (2019), is required to understand which of these variables are the predominant drivers of phytoplankton size variability in the NES region.

Absorption-based algorithms are advantageous over abundance-based methods in that they are rooted in a direct spectral response to phytoplankton cell size, as opposed to relying on indirect statistical connections between [*Chl-a*] and phytoplankton size structure. This means that they enable detection of changes in PSCs that occur outside

of the general biomass-size co-variation relationship and are less prone to change temporally or geographically. When applied directly to the satellite data, the two absorption-based algorithms examined in this study performed with comparable accuracy to the regionalized abundance-based models. The MY10 algorithm showed statistically similar performance to the *SST*-dependent model, without the inclusion of additional environmental information. Considering that pigment-based size class estimates from DPA were used for validation, the similarity in performance for the absorption-based algorithms is encouraging given they were not developed or parameterized using DPA, as was the case with the abundance-based methods. This suggests consistency between estimates of PSCs derived from spectral phytoplankton absorption and those determined from HPLC pigment analysis in the NES, as has been previously reported in other regions (Devred et al., 2011). Moreover, as they are not solely reliant on [*Chl-a*] for deriving size, the satellite-estimated C_{size} from the absorption-based approaches did not suffer from the same bias at high and low [*Chl-a*] inherent in the OC-CCI [*Chl-a*]. Nevertheless, as is the case with abundance-based approaches, any biases in satellite $a_{ph}(\lambda)$ or $a_{dg}(\lambda)$ used as input will be directly translated to the PSC output. Despite their strengths, the absorption-based methods were unable to characterize areas where $a_{ph}(\lambda)$ retrievals were poor (negative $a_{ph}(555)$ in the case of the CO2 model) or, in the case of the MY10 model, where [*Chl-a*] and $a_{dg}(443)$ were outside of set thresholds. These issues will be more prevalent in optically complex waters such as the NES and may be a drawback to the use of these algorithms in regions of high biomass or large relative optical contribution of CDOM and NAP.

While less common than abundance-based and absorption-based methods and outside of the focus of this study, approaches that exploit satellite backscattering data to derive PSCs have also been developed (Kostadinov et al., 2016, 2009; Montes-Hugo et al., 2008). These "backscattering-based" methods share many of the same advantages of absorption-based algorithms, as they utilize the direct spectral response of in-water constituents and are less reliant on empirical relationships, making them less susceptible to ecological shifts in a changing ocean. However, current approaches estimate PSCs under the assumption that the particle assemblage is totally biogenic in nature, an assumption that generally holds in the open ocean but can be violated in coastal systems where inorganic particles are introduced through processes such as river discharge and tidal mixing (Kostadinov et al., 2016). Nonetheless, backscattering information provides an important tool for remotely estimating the size structure of phytoplankton communities and its use in combination with methods based on other optical and environmental data has potential to greatly improve PSC retrievals.

The PSC algorithms and products evaluated in this study may be useful for the validation or assimilation of regional ecosystem or biogeochemical models (IOCCG, 2020). However, given the uncertainties associated with the pigment-based size class estimates used for algorithm assessment, as well as the different inputs and outputs between methods, it is difficult to make a definitive determination of which approach is the best choice for such applications. The most suitable method may be dependent on the specifics of the intended application or the questions to be addressed. For instance, biogeochemical models that produce chlorophyll-based phytoplankton size estimates may prefer to compare to abundance-based algorithm outputs, while models that include

optics may prefer to compare to output from absorption-based methods – each enabling a more direct comparison depending on the underlying algorithm/model frameworks and outputs being compared.

In the near future, satellite ocean color remote sensing is moving toward more advanced radiometric instruments with hyperspectral capability and enhanced spatial and temporal resolution (Cetinić et al., 2018). The increased spectral information afforded by these upcoming sensors is anticipated to greatly improve our ability to accurately separate the absorption attributed to different optically significant in-water constituents (i.e., CDOM, NAP, phytoplankton) and retrieve information on phytoplankton community composition and size structure. This improved capability will be particularly relevant to optically complex waters, including coastal and continental shelf regions like the NES ecosystem. Thus, existing absorption-based PSC models may potentially become more robust, and newer methods that exploit the full range of available spectral information will continue to be developed. Furthermore, to the extent that satellite [*Chl-a*] estimates improve as a result of the increase in spectral resolution, abundance-based approaches may continue to be an effective option for estimating PSCs, especially when combined with *SST* or other ecologically relevant environmental parameters. While not considered in this work, the integration of high-resolution spectral information with environmental data readily attainable from remote sensing should be considered in future PSC algorithm development efforts.

5. References

Bailey, S.W., Werdell, P.J., 2006. A multi-sensor approach for the on-orbit validation of ocean color satellite data products. Remote Sens. Environ. 102, 12–23. https://doi.org/10.1016/j.rse.2006.01.015

Behrenfeld, M.J., O'Malley, R.T., Siegel, D.A., McClain, C.R., Sarmiento, J.L., Feldman, G.C., Milligan, A.J., Falkowski, P.G., Letelier, R.M., Boss, E.S., 2006. Climate- driven trends in contemporary ocean productivity. Nat. Lond. 444, 752–5. http://dx.doi.org.uri.idm.oclc.org/10.1038/nature05317

Bouman, H.A., Platt, T., Sathyendranath, S., Li, W.K.W., Stuart, V., Fuentes-Yaco, C., Maass, H., Horne, E.P.W., Ulloa, O., Lutz, V., Kyewalyanga, M., 2003. Temperature as indicator of optical properties and community structure of marine phytoplankton: implications for remote sensing. Mar. Ecol. Prog. Ser. 258, 19–30.

Boyce, D.G., Frank, K.T., Leggett, W.C., 2015. From mice to elephants: overturning the 'one size fits all' paradigm in marine plankton food chains. Ecol. Lett. 18, 504–515. https://doi.org/10.1111/ele.12434

Brewin, R.J.W., Brewin, R.J.W., Morán, X.A.G., Raitsos, D.E., Raitsos, D.E., Gittings, J.A., Calleja, M.L., Calleja, M.L., Viegas, M., Ansari, M.I., Al-Otaibi, N., Huete-Stauffer, T.M., Hoteit, I., 2019. Factors Regulating the Relationship Between Total and Size-

Fractionated Chlorophyll-a in Coastal Waters of the Red Sea. Front. Microbiol. 10. https://doi.org/10.3389/fmicb.2019.01964

Brewin, R.J.W., Ciavatta, S., Sathyendranath, S., Jackson, T., Tilstone, G., Curran, K., Airs, R.L., Cummings, D., Brotas, V., Organelli, E., Dall'Olmo, G., Raitsos, D.E., 2017a. Uncertainty in Ocean-Color Estimates of Chlorophyll for Phytoplankton Groups. Front. Mar. Sci. 4. https://doi.org/10.3389/fmars.2017.00104

Brewin, R.J.W., Ciavatta, S., Sathyendranath, S., Jackson, T., Tilstone, G., Curran, K., Airs, R.L., Cummings, D., Brotas, V., Organelli, E., Dall'Olmo, G., Raitsos, D.E., 2017b. Uncertainty in Ocean-Color Estimates of Chlorophyll for Phytoplankton Groups. Front. Mar. Sci. 4. https://doi.org/10.3389/fmars.2017.00104

Brewin, R.J.W., Hardman-Mountford, N.J., Lavender, S.J., Raitsos, D.E., Hirata, T., Uitz, J., Devred, E., Bricaud, A., Ciotti, A., Gentili, B., 2011. An intercomparison of bio-optical techniques for detecting dominant phytoplankton size class from satellite remote sensing. Remote Sens. Environ. 115, 325–339. https://doi.org/10.1016/j.rse.2010.09.004

Brewin, R.J.W., Sathyendranath, S., Hirata, T., Lavender, S.J., Barciela, R.M., Hardman-Mountford, N.J., 2010. A three-component model of phytoplankton size class for the Atlantic Ocean. Ecol. Model. 221, 1472–1483. https://doi.org/10.1016/j.ecolmodel.2010.02.014

Brewin, R.J.W., Sathyendranath, S., Jackson, T., Barlow, R., Brotas, V., Airs, R., Lamont, T., 2015. Influence of light in the mixed-layer on the parameters of a three-component model of phytoplankton size class. Remote Sens. Environ. 168, 437–450. https://doi.org/10.1016/j.rse.2015.07.004

Brewin, Sathyendranath, S., Müller, D., Brockmann, C., Deschamps, P.-Y., Devred, E., Doerffer, R., Fomferra, N., Franz, B., Grant, M., Groom, S., Horseman, A., Hu, C., Krasemann, H., Lee, Z., Maritorena, S., Mélin, F., Peters, M., Platt, T., Regner, P., Smyth, T., Steinmetz, F., Swinton, J., Werdell, J., White, G.N., 2015. The Ocean Colour Climate Change Initiative: III. A round-robin comparison on in-water bio-optical algorithms. Remote Sens. Environ. 162, 271–294. https://doi.org/10.1016/j.rse.2013.09.016

Bricaud, A., Bédhomme, A.-L., Morel, A., 1988. Optical properties of diverse phytoplanktonic species: experimental results and theoretical interpretation. J. Plankton Res. 10, 851–873. https://doi.org/10.1093/plankt/10.5.851

Bricaud, A., Claustre, H., Ras, J., Oubelkheir, K., 2004. Natural variability of phytoplanktonic absorption in oceanic waters: Influence of the size structure of algal populations. J. Geophys. Res. Oceans 109. https://doi.org/10.1029/2004JC002419

Brito, A.C., Sá, C., Brotas, V., Brewin, R.J.W., Silva, T., Vitorino, J., Platt, T., Sathyendranath, S., 2015. Effect of phytoplankton size classes on bio-optical properties of phytoplankton in the Western Iberian coast: Application of models. Remote Sens. Environ. 156, 537–550. https://doi.org/10.1016/j.rse.2014.10.020

Caron, D.A., Countway, P.D., Jones, A.C., Kim, D.Y., Schnetzer, A., 2012. Marine Protistan Diversity. Annu. Rev. Mar. Sci. 4, 467–493. https://doi.org/10.1146/annurev-marine-120709-142802

Cetinić, I., McClain, C.R., Werdell, P.J., 2018. PACE Technical Report Series 2, 316.

Chase, A.P., Kramer, S.J., Haëntjens, N., Boss, E.S., Karp-Boss, L., Edmondson, M., Graff, J.R., 2020. Evaluation of diagnostic pigments to estimate phytoplankton size classes. Limnol. Oceanogr. Methods n/a. https://doi.org/10.1002/lom3.10385

Chin, T.M., Vazquez-Cuervo, J., Armstrong, E.M., 2017. A multi-scale high-resolution analysis of global sea surface temperature. Remote Sens. Environ. 200, 154–169. https://doi.org/10.1016/j.rse.2017.07.029

Chisholm, S.W., Olson, R.J., Zettler, E.R., Goericke, R., Waterbury, J.B., Welschmeyer, N.A., 1988. A novel free-living prochlorophyte abundant in the oceanic euphotic zone. Nature 334, 340–343. https://doi.org/10.1038/334340a0

Ciotti, A.M., Bricaud, A., 2006. Retrievals of a size parameter for phytoplankton and spectral light absorption by colored detrital matter from water-leaving radiances at SeaWiFS channels in a continental shelf region off Brazil: Algal size and CDM from SeaWiFS data. Limnol. Oceanogr. Methods 4, 237–253. https://doi.org/10.4319/lom.2006.4.237

Ciotti, Á.M., Lewis, M.R., Cullen, J.J., 2002. Assessment of the relationships between dominant cell size in natural phytoplankton communities and the spectral shape of the absorption coefficient. Limnol. Oceanogr. 47, 404–417. https://doi.org/10.4319/lo.2002.47.2.0404

Claustre, H., 2005. Toward a taxon-specific parameterization of bio-optical models of primary production: A case study in the North Atlantic. J. Geophys. Res. 110. https://doi.org/10.1029/2004JC002634

Devred, E., Sathyendranath, S., Stuart, V., Maass, H., Ulloa, O., Platt, T., 2006. A two-component model of phytoplankton absorption in the open ocean: Theory and applications. J. Geophys. Res. Oceans 111. https://doi.org/10.1029/2005JC002880

Devred, E., Sathyendranath, S., Stuart, V., Platt, T., 2011. A three component classification of phytoplankton absorption spectra: Application to ocean-color data. Remote Sens. Environ. 115, 2255–2266. https://doi.org/10.1016/j.rse.2011.04.025

Di Cicco, A., Sammartino, M., Marullo, S., Santoleri, R., 2017. Regional Empirical Algorithms for an Improved Identification of Phytoplankton Functional Types and Size Classes in the Mediterranean Sea Using Satellite Data. Front. Mar. Sci. 4. https://doi.org/10.3389/fmars.2017.00126

Dierssen, H.M., 2010. Perspectives on empirical approaches for ocean color remote sensing of chlorophyll in a changing climate. Proc. Natl. Acad. Sci. 107, 17073–17078. https://doi.org/10.1073/pnas.0913800107

Estrella, E.H., Groetsch, P., Gilerson, A., Malinowski, M., Ahmed, S., n.d. Blue band reflectance uncertainties in coastal waters and their impact on retrieval algorithms 14.

Field, C.B., Behrenfeld, M.J., Randerson, J.T., Falkowski, P., 1998. Primary Production of the Biosphere: Integrating Terrestrial and Oceanic Components. Science 281, 237–240.

Finkel, Z.V., Beardall, J., Flynn, K.J., Quigg, A., Rees, T.A.V., Raven, J.A., 2010. Phytoplankton in a changing world: cell size and elemental stoichiometry. J. Plankton Res. 32, 119–137. https://doi.org/10.1093/plankt/fbp098

Friedland, K.D., Langan, J.A., Large, S.I., Selden, R.L., Link, J.S., Watson, R.A., Collie, J.S., 2020. Changes in higher trophic level productivity, diversity and niche space in a rapidly warming continental shelf ecosystem. Sci. Total Environ. 704, 135270. https://doi.org/10.1016/j.scitotenv.2019.135270

Friedland, K.D., Record, N.R., Asch, R.G., Kristiansen, T., Saba, V.S., Drinkwater, K.F., Henson, S., Leaf, R.T., Morse, R.E., Johns, D.G., Large, S.I., Hjøllo, S.S., Nye, J.A., Alexander, M.A., Ji, R., 2016. Seasonal phytoplankton blooms in the North Atlantic linked to the overwintering strategies of copepods. Elem Sci Anth 4, 000099. https://doi.org/10.12952/journal.elementa.000099

Gittings, J.A., Brewin, R.J.W., Raitsos, D.E., Kheireddine, M., Ouhssain, M., Jones, B.H., Hoteit, I., 2019. Remotely sensing phytoplankton size structure in the Red Sea. Remote Sens. Environ. 234, 111387. https://doi.org/10.1016/j.rse.2019.111387

Gohin, F., Druon, J.N., Lampert, L., 2002. A five channel chlorophyll concentration algorithm applied to SeaWiFS data processed by SeaDAS in coastal waters. Int. J. Remote Sens. 23, 1639–1661. https://doi.org/10.1080/01431160110071879

Grunert, B.K., Mouw, C.B., Ciochetto, A.B., 2019. Deriving inherent optical properties from decomposition of hyperspectral non-water absorption. Remote Sens. Environ. 225, 193–206. https://doi.org/10.1016/j.rse.2019.03.004

Guidi, L., Stemmann, L., Jackson, G.A., Ibanez, F., Claustre, H., Legendre, L., Picheral, M., Gorskya, G., 2009. Effects of phytoplankton community on production, size, and export of large aggregates: A world-ocean analysis. Limnol. Oceanogr. 54, 1951–1963. https://doi.org/10.4319/lo.2009.54.6.1951

Hare, J.A., Morrison, W.E., Nelson, M.W., Stachura, M.M., Teeters, E.J., Griffis, R.B., Alexander, M.A., Scott, J.D., Alade, L., Bell, R.J., Chute, A.S., Curti, K.L., Curtis, T.H., Kircheis, D., Kocik, J.F., Lucey, S.M., McCandless, C.T., Milke, L.M., Richardson, D.E., Robillard, E., Walsh, H.J., McManus, M.C., Marancik, K.E., Griswold, C.A., 2016. A Vulnerability Assessment of Fish and Invertebrates to Climate Change on the Northeast U.S. Continental Shelf. PLOS ONE 11, e0146756. https://doi.org/10.1371/journal.pone.0146756

Hirata, T., Hardman-Mountford, N.J., Brewin, R.J.W., Aiken, J., Barlow, R., Suzuki, K., Isada, T., Howell, E., Hashioka, T., Noguchi-Aita, M., Yamanaka, Y., 2011. Synoptic relationships between surface Chlorophyll-*a* and diagnostic pigments specific to phytoplankton functional types. Biogeosciences 8, 311–327. https://doi.org/10.5194/bg-8-311-2011

Hu, C., Lee, Z., Franz, B., 2012. Chlorophyll aalgorithms for oligotrophic oceans: A novel approach based on three-band reflectance difference. J. Geophys. Res. Oceans 117. https://doi.org/10.1029/2011JC007395

Hunter-Cevera, K.R., Neubert, M.G., Olson, R.J., Solow, A.R., Shalapyonok, A., Sosik, H.M., 2016. Physiological and ecological drivers of early spring blooms of a coastal phytoplankter. Science 354, 326–329. https://doi.org/10.1126/science.aaf8536

IOCCG, 2020. Synergy between Ocean Colour and Biogeochemical/ Ecosystem Models. IOCCG, Dartmouth, Canada.

IOCCG, 2014. Phytoplankton Functional Types from Space. Sathyendranath, S. (ed.), Reports of the International Ocean-Colour Coordinating Group, No. 15. IOCCG, Dartmouth, Canada.

Jackson, T., Sathyendranath, S., Mélin, F., 2017. An improved optical classification scheme for the Ocean Colour Essential Climate Variable and its applications. Remote Sens. Environ., Earth Observation of Essential Climate Variables 203, 152–161. https://doi.org/10.1016/j.rse.2017.03.036

Kleisner, K.M., Fogarty, M.J., McGee, S., Hare, J.A., Moret, S., Perretti, C.T., Saba, V.S., 2017. Marine species distribution shifts on the U.S. Northeast Continental Shelf under continued ocean warming. Prog. Oceanogr. 153, 24–36. https://doi.org/10.1016/j.pocean.2017.04.001

Kostadinov, T.S., Cabré, A., Vedantham, H., Marinov, I., Bracher, A., Brewin, R.J.W., Bricaud, A., Hirata, T., Hirawake, T., Hardman-Mountford, N.J., Mouw, C., Roy, S., Uitz, J., 2017. Inter-comparison of phytoplankton functional type phenology metrics derived from ocean color algorithms and Earth System Models. Remote Sens. Environ. 190, 162–177. https://doi.org/10.1016/j.rse.2016.11.014

Kostadinov, T.S., Milutinović, S., Marinov, I., Cabré, A., 2016. Carbon-based phytoplankton size classes retrieved via ocean color estimates of the particle size distribution. Ocean Sci. 12, 561–575. https://doi.org/10.5194/os-12-561-2016

Kostadinov, T.S., Siegel, D.A., Maritorena, S., 2009. Retrieval of the particle size distribution from satellite ocean color observations. J. Geophys. Res. Oceans 114. https://doi.org/10.1029/2009JC005303

Laws, E.A., Archie, J.W., 1981. Appropriate use of regression analysis in marine biology. Mar. Biol. 65, 13–16. https://doi.org/10.1007/BF00397062

Le Quéré, C.L., Harrison, S.P., Prentice, I.C., Buitenhuis, E.T., Aumont, O., Bopp, L., Claustre, H., Cunha, L.C.D., Geider, R., Giraud, X., Klaas, C., Kohfeld, K.E., Legendre, L., Manizza, M., Platt, T., Rivkin, R.B., Sathyendranath, S., Uitz, J., Watson, A.J., Wolf-Gladrow, D., 2005. Ecosystem dynamics based on plankton functional types for global ocean biogeochemistry models. Glob. Change Biol. 11, 2016–2040. https://doi.org/10.1111/j.1365-2486.2005.1004.x

Leblanc, K., Quéguiner, B., Diaz, F., Cornet, V., Michel-Rodriguez, M., Durrieu de Madron, X., Bowler, C., Malviya, S., Thyssen, M., Grégori, G., Rembauville, M., Grosso, O., Poulain, J., de Vargas, C., Pujo-Pay, M., Conan, P., 2018. Nanoplanktonic diatoms

are globally overlooked but play a role in spring blooms and carbon export. Nat. Commun. 9, 953. https://doi.org/10.1038/s41467-018-03376-9

Lee, Z., Lubac, B., Werdell, J., Arnone, R., 2009. An Update of the Quasi-Analytical Algorithm (QAA_v5). International Ocean Colour Coordinating Group (IOCCG).

Liu, X., Devred, E., Johnson, C., 2018. Remote Sensing of Phytoplankton Size Class in Northwest Atlantic from 1998 to 2016: Bio-Optical Algorithms Comparison and Application. Remote Sens. 10, 1028. https://doi.org/10.3390/rs10071028

Mackey, M., Mackey, D., Higgins, H., Wright, S., 1996. CHEMTAX - a program for estimating class abundances from chemical markers:application to HPLC measurements of phytoplankton. Mar. Ecol. Prog. Ser. 144, 265–283. https://doi.org/10.3354/meps144265

Mannino, A., Novak, M.G., Hooker, S.B., Hyde, K., Aurin, D., 2014. Algorithm development and validation of CDOM properties for estuarine and continental shelf waters along the northeastern U.S. coast. Remote Sens. Environ. 152, 576–602. https://doi.org/10.1016/j.rse.2014.06.027

Marañón, E., 2015. Cell Size as a Key Determinant of Phytoplankton Metabolism and Community Structure. Annu. Rev. Mar. Sci. 7, 241–264. https://doi.org/10.1146/annurev-marine-010814-015955

Margalef, R., 1978. Life-forms of phytoplankton as survival alternatives in an unstable environment. Oceanol. Acta.

Marinov, I., Doney, S.C., Lima, I.D., 2010. Response of ocean phytoplankton community structure to climate change over the 21st century: partitioning the effects of nutrients, temperature and light. Biogeosciences 7, 3941–3959. https://doi.org/10.5194/bg-7-3941-2010

Mobley, C.D., Sundman, L.K., 2013. HYDROLIGHT 5.2 ECOLIGHT 5.2 Technical Documentation.

Montes-Hugo, M.A., Vernet, M., Smith, R., Carder, K., 2008. Phytoplankton size-structure on the western shelf of the Antarctic Peninsula: a remote-sensing approach. Int. J. Remote Sens. 29, 801–829. https://doi.org/10.1080/01431160701297615

Moore, T.S., Brown, C.W., 2020. Incorporating environmental data in abundance-based algorithms for deriving phytoplankton size classes in the Atlantic Ocean. Remote Sens. Environ. 240, 111689. https://doi.org/10.1016/j.rse.2020.111689

Moore, T.S., Campbell, J.W., Dowell, M.D., 2009. A class-based approach to characterizing and mapping the uncertainty of the MODIS ocean chlorophyll product. Remote Sens. Environ. 113, 2424–2430. https://doi.org/10.1016/j.rse.2009.07.016

Morán, X.A.G., López-Urrutia, Á., Calvo-Díaz, A., Li, W.K.W., 2010. Increasing importance of small phytoplankton in a warmer ocean. Glob. Change Biol. 16, 1137–1144. https://doi.org/10.1111/j.1365-2486.2009.01960.x

Morel, A., 1987. Chlorophyll-specific scattering coefficient of phytoplankton. A simplified theoretical approach. Deep Sea Res. Part Oceanogr. Res. Pap. 34, 1093–1105. https://doi.org/10.1016/0198-0149(87)90066-5

Morel, A., Bricaud, A., 1981. Theoretical results concerning light absorption in a discrete medium, and application to specific absorption of phytoplankton. Deep Sea Res. Part Oceanogr. Res. Pap. 28, 1375–1393. https://doi.org/10.1016/0198-0149(81)90039-X

Mouw, C.B., Barnett, A., McKinley, G.A., Gloege, L., Pilcher, D., 2016. Phytoplankton size impact on export flux in the global ocean. Glob. Biogeochem. Cycles 30, 1542–1562. https://doi.org/10.1002/2015GB005355

Mouw, C.B., Ciochetto, A.B., Grunert, B., Yu, A., 2017a. Expanding understanding of optical variability in Lake Superior with a 4-year dataset. Earth Syst. Sci. Data 9, 497–509. https://doi.org/10.5194/essd-9-497-2017

Mouw, C.B., Ciochetto, A.B., Yoder, J.A., 2019. A Satellite Assessment of Environmental Controls of Phytoplankton Community Size Structure. Glob. Biogeochem. Cycles 33, 540–558. https://doi.org/10.1029/2018GB006118

Mouw, C.B., Hardman-Mountford, N.J., Alvain, S., Bracher, A., Brewin, R.J.W., Bricaud, A., Ciotti, A.M., Devred, E., Fujiwara, A., Hirata, T., Hirawake, T., Kostadinov, T.S., Roy, S., Uitz, J., 2017b. A Consumer's Guide to Satellite Remote Sensing of Multiple Phytoplankton Groups in the Global Ocean. Front. Mar. Sci. 4. https://doi.org/10.3389/fmars.2017.00041

Mouw, C.B., Yoder, J.A., 2010. Optical determination of phytoplankton size composition from global SeaWiFS imagery. J. Geophys. Res. 115. https://doi.org/10.1029/2010JC006337

Mouw, C.B., Yoder, J.A., Doney, S.C., 2012. Impact of phytoplankton community size on a linked global ocean optical and ecosystem model. J. Mar. Syst. 89, 61–75. https://doi.org/10.1016/j.jmarsys.2011.08.002

Mueller, J.L., Fargion, G.S., McClain, C.R., 2003. Ocean Optics Protocols for Satellite Ocean Color Sensor Validation (No. TM-2003-211621/Rev4-Vol.IV). NASA, Greenbelt, MD, USA.

Nair, A., Sathyendranath, S., Platt, T., Morales, J., Stuart, V., Forget, M.-H., Devred, E., Bouman, H., 2008. Remote sensing of phytoplankton functional types. Remote Sens. Environ., Earth Observations for Marine and Coastal Biodiversity and Ecosystems Special Issue 112, 3366–3375. https://doi.org/10.1016/j.rse.2008.01.021

National Marine Fisheries Service (Ed.), 2020. Cruise Results: NOAA Research Vessel GORDON GUNTER, Cruise No. GU 19-05, Fall Northeast Ecosystem Monitoring Survey. https://doi.org/10.25923/ah4q-2b94

National Marine Fisheries Service, 2018. Fisheries Economics of the United States 2016 (NOAA Tech. Memo No. NMFS-F/SPO-187a). U.S. Department of Commerce.

Nunes, S., Perez, G.L., Latasa, M., Zamanillo, M., Delgado, M., Ortega-Retuerta, E., Marrasé, C., Simó, R., Estrada, M., 2019. Size fractionation, chemotaxonomic groups and bio-optical properties of phytoplankton along a transect from the Mediterranean Sea to the SW Atlantic Ocean. Sci. Mar. 83, 87. https://doi.org/10.3989/scimar.04866.10A

Olson, R.J., Sosik, H.M., 2007. A submersible imaging-in-flow instrument to analyze nano-and microplankton: Imaging FlowCytobot. Limnol. Oceanogr. Methods 5, 195–203. https://doi.org/10.4319/lom.2007.5.195

O'Reilly, J.E., Maritorena, S., Mitchell, B.G., Siegel, D.A., Carder, K.L., Garver, S.A., Kahru, M., McClain, C., 1998. Ocean color chlorophyll algorithms for SeaWiFS. J. Geophys. Res. Oceans 103, 24937–24953. https://doi.org/10.1029/98JC02160

O'Reilly, J.E., Zetlin, C., 1998. Seasonal, Horizonal, and Vertical Distribution of Phytoplankton Chlorophyll a in the Northeast U.S. Continental Shelf Ecosystem. NOAA National Marine Fisheries Service.

Pan, X., Mannino, A., Marshall, H.G., Filippino, K.C., Mulholland, M.R., 2011. Remote sensing of phytoplankton community composition along the northeast coast of the

United States. Remote Sens. Environ. 115, 3731–3747. https://doi.org/10.1016/j.rse.2011.09.011

Pan, X., Mannino, A., Russ, M.E., Hooker, S.B., 2008. Remote sensing of the absorption coefficients and chlorophyll a concentration in the United States southern Middle Atlantic Bight from SeaWiFS and MODIS-Aqua. J. Geophys. Res. Oceans 113. https://doi.org/10.1029/2008JC004852

Pan, X., Mannino, A., Russ, M.E., Hooker, S.B., Harding, L.W., 2010. Remote sensing of phytoplankton pigment distribution in the United States northeast coast. Remote Sens. Environ. 114, 2403–2416. https://doi.org/10.1016/j.rse.2010.05.015

Pershing, A.J., Alexander, M.A., Hernandez, C.M., Kerr, L.A., Bris, A.L., Mills, K.E., Nye, J.A., Record, N.R., Scannell, H.A., Scott, J.D., Sherwood, G.D., Thomas, A.C., 2015. Slow adaptation in the face of rapid warming leads to collapse of the Gulf of Maine cod fishery. Science 350, 809–812. https://doi.org/10.1126/science.aac9819

Platt, T., Sathyendranath, S., 2008. Ecological indicators for the pelagic zone of the ocean from remote sensing. Remote Sens. Environ., Earth Observations for Marine and Coastal Biodiversity and Ecosystems Special Issue 112, 3426–3436. https://doi.org/10.1016/j.rse.2007.10.016

Raven, J.A., 1998. The twelfth Tansley Lecture. Small is beautiful: the picophytoplankton. Funct. Ecol. 12, 503–513. https://doi.org/10.1046/j.1365-2435.1998.00233.x

Richaud, B., Kwon, Y.-O., Joyce, T.M., Fratantoni, P.S., Lentz, S.J., 2016. Surface and bottom temperature and salinity climatology along the continental shelf off the Canadian and U.S. East Coasts. Cont. Shelf Res. 124, 165–181. https://doi.org/10.1016/j.csr.2016.06.005

Roy, S., 2011. Phytoplankton Pigments : Characterization, Chemotaxonomy and Applications in Oceanography, Cambridge Environmental Chemistry Series. Cambridge University Press, Cambridge.

Saba, V.S., Hyde, K.J.W., Rebuck, N.D., Friedland, K.D., Hare, J.A., Kahru, M., Fogarty, M.J., 2015. Physical associations to spring phytoplankton biomass interannual variability in the U.S. Northeast Continental Shelf. J. Geophys. Res. Biogeosciences 120, 205–220. https://doi.org/10.1002/2014JG002770

Sathyendranath, S., Brewin, R.J.W., Brockmann, C., Brotas, V., Calton, B., Chuprin, A., Cipollini, P., Couto, A.B., Dingle, J., Doerffer, R., Donlon, C., Dowell, M., Farman, A., Grant, M., Groom, S., Horseman, A., Jackson, T., Krasemann, H., Lavender, S., Martinez-Vicente, V., Mazeran, C., Mélin, F., Moore, T.S., Müller, D., Regner, P., Roy, S., Steele, C.J., Steinmetz, F., Swinton, J., Taberner, M., Thompson, A., Valente, A., Zühlke, M., Brando, V.E., Feng, H., Feldman, G., Franz, B.A., Frouin, R., Gould, R.W., Hooker, S.B., Kahru, M., Kratzer, S., Mitchell, B.G., Muller-Karger, F.E., Sosik, H.M., Voss, K.J., Werdell, J., Platt, T., 2019. An Ocean-Colour Time Series for Use in Climate Studies: The Experience of the Ocean-Colour Climate Change Initiative (OC-CCI). Sensors 19, 4285. https://doi.org/10.3390/s19194285

Sathyendranath, S., Cota, G., Stuart, V., Maass, H., Platt, T., 2001. Remote sensing of phytoplankton pigments: A comparison of empirical and theoretical approaches. Int. J. Remote Sens. 22, 249–273. https://doi.org/10.1080/014311601449925

Sauer, M.J., Roesler, C.S., Werdell, P.J., Barnard, A., 2012. Under the hood of satellite empirical chlorophyll a algorithms: revealing the dependencies of maximum band ratio algorithms on inherent optical properties. Opt. Express 20, 20920. https://doi.org/10.1364/OE.20.020920

Schollaert, S.E., Rossby, T., Yoder, J.A., 2004. Gulf Stream cross-frontal exchange: possible mechanisms to explain interannual variations in phytoplankton chlorophyll in the Slope Sea during the SeaWiFS years. Deep Sea Res. Part II Top. Stud. Oceanogr. 51, 173–188. https://doi.org/10.1016/j.dsr2.2003.07.017

Seegers, B.N., Stumpf, R.P., Schaeffer, B.A., Loftin, K.A., Werdell, P.J., 2018. Performance metrics for the assessment of satellite data products: an ocean color case study. Opt. Express 26, 7404–7422.

Sieburth, J.McN., Smetacek, V., Lenz, J., 1978. Pelagic ecosystem structure: Heterotrophic compartments of the plankton and their relationship to plankton size fractions 1. Limnol. Oceanogr. 23, 1256–1263. https://doi.org/10.4319/lo.1978.23.6.1256

Sun, X., Shen, F., Brewin, R.J.W., Liu, D., Tang, R., 2019a. Twenty-Year Variations in Satellite-Derived Chlorophyll-a and Phytoplankton Size in the Bohai Sea and Yellow Sea. J. Geophys. Res. Oceans 124, 8887–8912. https://doi.org/10.1029/2019JC015552

Sun, X., Shen, F., Brewin, R.J.W., Liu, D., Tang, R., 2019b. Twenty-Year Variations in Satellite-Derived Chlorophyll-a and Phytoplankton Size in the Bohai Sea and Yellow Sea. J. Geophys. Res. Oceans 124, 8887–8912. https://doi.org/10.1029/2019JC015552

Sun, X., Shen, F., Liu, D., Bellerby, R.G.J., Liu, Y., Tang, R., 2018. In Situ and Satellite Observations of Phytoplankton Size Classes in the Entire Continental Shelf Sea, China. J. Geophys. Res. Oceans 123, 3523–3544. https://doi.org/10.1029/2017JC013651

Torrecilla, E., Stramski, D., Reynolds, R.A., Millán-Núñez, E., Piera, J., 2011. Cluster analysis of hyperspectral optical data for discriminating phytoplankton pigment assemblages in the open ocean. Remote Sens. Environ. 115, 2578–2593. https://doi.org/10.1016/j.rse.2011.05.014

Trees, C.C., Clark, D.K., Bidigare, R.R., Ondrusek, M.E., Mueller, J.L., 2000. Accessory pigments versus chlorophyll a concentrations within the euphotic zone: A ubiquitous relationship. Limnol. Oceanogr. 45, 1130–1143. https://doi.org/10.4319/lo.2000.45.5.1130

Uitz, J., Claustre, H., Morel, A., Hooker, S.B., 2006. Vertical distribution of phytoplankton communities in open ocean: An assessment based on surface chlorophyll. J. Geophys. Res. Oceans 111. https://doi.org/10.1029/2005JC003207

Uitz, J.U., Huot, Y., Bruyant, F., Babin, M., Claustre, H., 2008. Relating phytoplankton photophysiological properties to community structure on large scales. Limnol. Oceanogr. 53, 614–630. https://doi.org/10.4319/lo.2008.53.2.0614

Vidussi, F., Claustre, H., Manca, B.B., Luchetta, A., Marty, J.-C., 2001. Phytoplankton pigment distribution in relation to upper thermocline circulation in the eastern Mediterranean Sea during winter. J. Geophys. Res. Oceans 106, 19939–19956. https://doi.org/10.1029/1999JC000308

Ward, B.A., 2015. Temperature-Correlated Changes in Phytoplankton Community Structure Are Restricted to Polar Waters. PLOS ONE 10, e0135581. https://doi.org/10.1371/journal.pone.0135581

Werdell, P.J., Franz, B.A., Bailey, S.W., Feldman, G.C., Boss, E., Brando, V.E., Dowell, M., Hirata, T., Lavender, S.J., Lee, Z., Loisel, H., Maritorena, S., Mélin, F., Moore, T.S., Smyth, T.J., Antoine, D., Devred, E., d'Andon, O.H.F., Mangin, A., 2013. Generalized ocean color inversion model for retrieving marine inherent optical properties. Appl. Opt. 52, 2019. https://doi.org/10.1364/AO.52.002019

Willmott, C.J., Matsuura, K., 2005. Advantages of the mean absolute error (MAE) over the root mean square error (RMSE) in assessing average model performance. Clim. Res. 30, 79–82.

Xu, F., Ignatov, A., 2014. In situ SST Quality Monitor (*i* Quam). J. Atmospheric Ocean. Technol. 31, 164–180. https://doi.org/10.1175/JTECH-D-13-00121.1

Yentsch, C.S., Phinney, D.A., 1989. A bridge between ocean optics and microbial ecology: Ocean optics and microbial ecology. Limnol. Oceanogr. 34, 1694–1705. https://doi.org/10.4319/lo.1989.34.8.1694

6. List of Figure and Table Captions

Table 1. Symbols and definitions.

Fig.1. Locations of the *in situ* data and satellite match-ups used in this study. The 200 and 2000 m isobaths from the 2019 General Bathymetric Chart of the Oceans (https://www.gebco.net/) are shown for reference. See Table 2 for information on data sources.

Table 2. Summary of *in situ* data sources. *N* denotes the number of samples (after QA) and the number in parentheses refers to the number of satellite match-ups. Citations for the individual data sets from SeaBASS are also provided.

Fig. 2. Relative frequencies of *in situ* observations from the NES data set used in this study (blue stairs): (a) HPLC-measured [*Chl-a*] (N = 786), (b) $a_{ph}(443)$ (N = 214) and (c) $a_{dg}(443)$ (N = 173), with their respective monthly distributions (d-f, black bars). Global distributions from an OC-CCI v4.2 annual satellite composite for 2018 are overlaid for comparison (red line). Frequencies were normalized by the maximum value.

Fig. 3. Comparison of the HPLC-measured [*Chl-a*] (C_{HPLC}) and the reconstructed [*Chl-a*] from the sum of seven diagnostic pigments (C_{DP}) using the weighting coefficients derived from this study (green circles; *MAD* = 0.12, *r* = 0.98), the weights derived by Uitz et al. (2006) from a global data set (blue triangles; *MAD* = 0.47, *r* = 0.96), and no weighting coefficients (magenta squares; *MAD* = 0.62, *r* = 0.96).

Table 3. Diagnostic pigments [***P***] and their associated taxonomic groups and attributed size classes, along with weighting coefficients [***W***] obtained from this study and previous studies. The number of data points and geographical regions of each study are also provided.

Table 4. Parameter values for the abundance-based models of Brewin et al. (2010) (Eqs. 9 and 10) and Hirata et al. (2011) (Eq. 16), obtained from this study and from previous studies.

Fig. 4. Brewin et al. (2010) model parameters (a) $C^m_{pico,nano}/C^m_{pico}$, and (b) $D_{pico,nano}/D_{pico}$ as a function of *SST*. Circle markers show the median parameter values obtained by performing a running bootstrap fit of the model (Eqs. 9 and 10) to the *in situ* parameterization data set (*N* = 418) sorted by increasing *SST*. The *SST*-parameter relationships were smoothed using a 5-point running average. Dashed lines indicate the *SST*-independent model (B-NES) parameters obtained when fitting the model to the full parameterization data set.

Fig. 5. Bivariate histograms showing the satellite-to-*in situ* comparisons of [*Chl-a*], $a_{ph}(\lambda)$, and $a_{dg}(\lambda)$, shaded by number of observations: (a) [*Chl-a*] from the standard OC-CCI algorithm, (b) [*Chl-a*] from the regional algorithm of Pan et al. (2010), (c) $a_{ph}(443)$, (d) $a_{ph}(490)$, (e) $a_{ph}(510)$, (f) $a_{dg}(443)$, (g) $a_{dg}(490)$, and (h) $a_{dg}(510)$ from the standard OC-CCI algorithm (QAA_v5). The solid black line is the 1:1 line, dashed black lines indicate the 1:1 line $\pm$ 30%, and the red line is the Type-II regression line. *N* denotes the number of match-ups, *MAD* denotes the mean absolute difference, δ denotes the bias, *r* denotes the correlation coefficient, and *S* denotes the regression slope. The $a_{ph}(\lambda)$ and $a_{dg}(\lambda)$ data are shown using the same x- and y-axis range for comparison.

Fig. 6. Pigment-based estimates of F_{size} (a-d) and C_{size} (e-h) as a function of C_{HPLC} from the parameterization data set (N = 418) with abundance-based models overlaid: re-parameterized B10 model (B-NES, solid black), re-parameterized H11 model (H-NES, dashed black), Brewin et al., 2010 (B10, blue), Brewin et al., 2015a (B15, green), Brewin et al., 2017 (B17, red), Devred et al., 2011 (D11, violet), Hirata et al., 2011 (H11, brown), and Moore and Brown, 2020 (MB20, yellow).

Fig. 7. Modeled F_{size} (a-d) and C_{size} (e-h) from the B-NES-*SST* model plotted as a function of [*Chl-a*], with the color gradient illustrating the changes in the model when model parameters vary as a function of *SST* (see Section 2.7.1.7, Fig. 4). The black line indicates the *SST*-independent model, with a single set of model parameters (B-NES).

Table 5. Mean absolute difference (*MAD*) and correlation coefficients (*r*) for F_{size} and C_{size} (values for C_{size} shown in parentheses) for the *SST*-dependent abundance-based models applied to the *in situ* parameterization and validation data sets. The percent change in the metrics when incorporating *SST* relative to the *SST*-independent models is included for reference. Percentages are rounded to the nearest 1%.

Fig. 8. Bivariate histograms showing the satellite-to-*in situ* comparisons of C_{size} estimated from the regionally parameterized B-NES-*SST* (a-d), B-NES (a-d), and H-NES (i-l) abundance-based models, shaded by number of observations. The solid black line is the 1:1 line, dashed black lines indicate the 1:1 line ± 30%, and the red line is the Type-II regression line. Dashed green lines indicate the maximum chlorophyll concentrations imposed by the B-NES model. *N* denotes the number of match-ups for each parameter, *MAD* denotes the mean absolute difference, δ denotes the bias, *r* denotes the correlation coefficient, and *S* denotes the regression slope.

Fig. 9. Bivariate histograms showing the satellite-to-*in situ* comparisons of C_{size} estimated from the absorption-based algorithms applied in this study: (a) $C_{micro,nano}$ and (b) C_{pico} from the algorithm of Ciotti et al. (2002) and (c) C_{micro} and (d) $C_{pico,nano}$ from the algorithm of Mouw and Yoder (2010). The solid black line is the 1:1 line, dashed black lines indicate the 1:1 line ± 30%, and the red line is the Type-II regression line. *N* denotes the number of match-ups, *MAD* denotes the mean absolute difference, δ denotes the bias, *r* denotes the correlation coefficient, and *S* denotes the regression slope.

Fig. 10. Monthly composite imagery for April 2019: (a) OC-CCI [*Chl-a*], (b) MUR *SST*, (c) F_{micro}, (d) F_{nano}, (e) F_{pico}, (f) C_{micro}, (g) C_{nano}, and (h) C_{pico} from the B-NES-*SST* model. Color scales for F_{size} are adjusted to reflect the range of the model for each size class (see Fig. 8). The black line indicates the 400 m isobath to mark the approximate location of the shelf break.

Fig. 11. Monthly composite imagery for September 2019: (a) OC-CCI [*Chl-a*], (b) MUR *SST*, (c) F_{micro}, (d) F_{nano}, (e) F_{pico}, (f) C_{micro}, (g) C_{nano}, and (h) C_{pico} from the B-NES-*SST* model, as per the previous figure.

Fig. 12. Comparison of monthly F_{micro} imagery from the B-NES-*SST* and MY10 algorithms for April 2019 (a, b) and September 2019 (c, d). The MY10 algorithm applies a 2-D average filter, masks pixels that exceed defined thresholds of [*Chl-a*] and $a_{dg}(443)$ (plotted in white), and bins F_{micro} to increments of 0.1 (see Section 2.7.2.2). The color scale for the B-NES-*SST* imagery was modified to match the output of the MY10 algorithm. The black line indicates the 400 m isobath to mark the approximate location of the shelf break.

7. Appendix A

Statistical metrics comparing the *in situ* pigment-based estimates of F_{size} and C_{size} from the parameterization and validation data sets with estimates from the abundance-based models shown in Figure 6. Statistical calculations were performed in linear space for F_{size} and $\log_{10}$ space for C_{size}. Metrics for C_{size} are shown in parentheses.

Parameter	Model	*in situ* training set (N = 418)			*in situ* validation set (N = 368)		
		MAD	δ	*r*	*MAD*	δ	*r*
F_{micro} (C_{micro})	B-NES	0.18 (0.24)	0.01 (0.11)	0.56 (0.86)	0.19 (0.25)	0.01 (0.13)	0.44 (0.85)
	H-NES	0.18 (0.21)	0.00 (0.10)	0.55 (0.86)	0.19 (0.25)	0.01 (0.12)	0.46 (0.85)
	B10	0.19 (0.24)	-0.08 (0.00)	0.56 (0.86)	0.21 (0.26)	-0.08 (0.01)	0.44 (0.85)
	B15	0.18 (0.24)	-0.02 (0.05)	0.56 (0.86)	0.20 (0.25)	-0.04 (0.05)	0.45 (0.85)
	B17	0.18 (0.24)	-0.02 (0.07)	0.56 (0.86)	0.19 (0.25)	-0.02 (0.08)	0.44 (0.85)
	D11	0.19 (0.24)	0.03 (0.10)	0.55 (0.86)	0.19 (0.25)	0.02 (0.09)	0.45 (0.85)
	H11	0.19 (0.25)	-0.06 (-0.02)	0.56 (0.86)	0.21 (0.25)	-0.08 (-0.04)	0.44 (0.85)
	MB20	0.19 (0.24)	-0.06 (0.04)	0.55 (0.86)	0.20 (0.25)	-0.05 (0.06)	0.45 (0.85)
$F_{pico,nano}$ ($C_{pico,nano}$)	B-NES	0.18 (0.19)	-0.01 (0.06)	0.56 (0.67)	0.19 (0.20)	-0.01 (0.06)	0.44 (0.72)
	H-NES	0.18 (0.19)	-0.01 (0.06)	0.55 (0.67)	0.19 (0.19)	-0.01 (0.07)	0.46 (0.73)
	B10	0.19 (0.21)	0.08 (0.14)	0.56 (0.67)	0.21 (0.22)	0.08 (0.14)	0.44 (0.72)
	B15	0.18 (0.20)	0.03 (0.09)	0.56 (0.66)	0.20 (0.21)	0.04 (0.10)	0.45 (0.71)
	B17	0.18 (0.19)	0.02 (0.08)	0.56 (0.66)	0.19 (0.20)	0.02 (0.09)	0.44 (0.71)
	D11	0.19 (0.20)	-0.03 (0.01)	0.55 (0.65)	0.19 (0.20)	-0.02 (0.03)	0.45 (0.70)
	H11	0.19 (0.22)	0.06 (0.09)	0.56 (0.47)	0.21 (0.22)	0.08 (0.12)	0.44 (0.68)
	MB20	0.19 (0.20)	0.06 (0.14)	0.55 (0.67)	0.20 (0.20)	0.05 (0.13)	0.45 (0.73)
F_{nano} (C_{nano})	B-NES	0.15 (0.24)	0.00 (0.10)	0.37 (0.66)	0.17 (0.28)	0.01 (0.13)	0.12 (0.74)
	H-NES	0.14 (0.24)	-0.01 (0.10)	0.38 (0.67)	0.16 (0.28)	0.00 (0.12)	0.16 (0.72)
	B10	0.18 (0.29)	0.12 (0.25)	0.37 (0.66)	0.21 (0.32)	0.13 (0.27)	0.20 (0.74)
	B15	0.15 (0.25)	0.05 (0.16)	0.38 (0.66)	0.17 (0.29)	0.05 (0.19)	0.20 (0.74)
	B17	0.15 (0.25)	0.04 (0.15)	0.37 (0.66)	0.17 (0.28)	0.04 (0.18)	0.20 (0.74)
	D11	0.14 (0.24)	-0.04 (0.02)	0.39 (0.65)	0.16 (0.26)	-0.04 (0.05)	0.21 (0.73)
	H11	0.16 (0.26)	0.02 (0.09)	0.36 (0.55)	0.19 (0.30)	0.04 (0.15)	0.10 (0.73)
	MB20	0.17 (0.27)	0.07 (0.21)	0.26 (0.67)	0.18 (0.29)	0.06 (0.21)	0.18 (0.74)
F_{pico} (C_{pico})	B-NES	0.08 (0.21)	-0.01 (0.05)	0.61 (0.55)	0.10 (0.22)	-0.02 (0.04)	0.63 (0.54)
	H-NES	0.07 (0.21)	0.00 (0.09)	0.67 (0.53)	0.09 (0.21)	-0.01 (0.07)	0.73 (0.59)
	B10	0.08 (0.25)	-0.04 (-0.10)	0.63 (0.40)	0.10 (0.25)	-0.04 (-0.08)	0.71 (0.40)
	B15	0.08 (0.24)	-0.02 (-0.04)	0.63 (0.41)	0.10 (0.24)	-0.02 (-0.01)	0.70 (0.42)
	B17	0.08 (0.24)	-0.02 (-0.04)	0.63 (0.43)	0.10 (0.24)	-0.02 (-0.02)	0.70 (0.43)
	D11	0.09 (0.24)	0.01 (0.03)	0.63 (0.40)	0.10 (0.24)	0.02 (0.05)	0.71 (0.40)
	H11	0.09 (0.25)	0.05 (0.19)	0.62 (0.52)	0.11 (0.25)	0.04 (0.17)	0.64 (0.51)
	MB20	0.08 (0.24)	-0.01 (-0.02)	0.63 (0.34)	0.10 (0.24)	-0.01 (0.01)	0.70 (0.38)